

NUMERICAL MODELING AND EXPERIMENTAL VALIDATION OF
GALVANIC CORROSION BETWEEN ALUMINUM ALLOY AA2024-T3 AND
CARBON FIBER REINFORCED PLASTIC CFRP

A THESIS SUBMITTED TO
THE GRADUATE SCHOOL OF NATURAL AND APPLIED SCIENCES
OF
MIDDLE EAST TECHNICAL UNIVERSITY

BY

MUSTAFA ANIL YILDIRIM

IN PARTIAL FULFILLMENT OF THE REQUIREMENTS
FOR
THE DEGREE OF MASTER OF SCIENCE
IN
METALLURGICAL AND MATERIALS ENGINEERING

JULY 2020

Approval of the thesis:

**NUMERICAL MODELING AND EXPERIMENTAL VALIDATION OF
GALVANIC CORROSION BETWEEN ALUMINUM ALLOY AA2024-T3
AND CARBON FIBER REINFORCED PLASTIC CFRP**

submitted by **MUSTAFA ANIL YILDIRIM** in partial fulfillment of the requirements
for the degree of **Master of Science in Metallurgical and Materials Engineering**
Department, Middle East Technical University by,

Prof. Dr. Halil Kalıpçılar
Dean, Graduate School of **Natural and Applied Sciences**

Prof. Dr. Cemil Hakan Gür
Head of Department, **Met. and Mat. Eng.**

Prof. Dr. İshak Karakaya
Supervisor, **Met. and Mat. Eng., METU**

Assist. Prof. Dr. Metehan Erdoğan
Co-Supervisor, **Materials Engineering Dept., AYBU**

Examining Committee Members:

Prof. Dr. Kadri Aydınol
Metallurgical and Materials Engineering Dept., METU

Prof. Dr. İshak Karakaya
Met. and Mat. Eng., METU

Assist. Prof. Dr. Metehan Erdoğan
Materials Eng. Dept., Ankara Yıldırım Beyazıt University

Assist. Prof. Dr. Batur Ercan
Metallurgical and Materials Engineering Dept., METU

Assist. Prof. Dr. Erkan Konca
Metallurgical and Materials Eng. Dept., Atılım University

Date: 27.07.2020

I hereby declare that all information in this document has been obtained and presented in accordance with academic rules and ethical conduct. I also declare that, as required by these rules and conduct, I have fully cited and referenced all material and results that are not original to this work.

Name, Surname: Mustafa Anıl Yıldırım

Signature:

ABSTRACT

NUMERICAL MODELING AND EXPERIMENTAL VALIDATION OF GALVANIC CORROSION BETWEEN ALUMINUM ALLOY AA2024-T3 AND CARBON FIBER REINFORCED PLASTIC CFRP

Yıldırım, Mustafa Anıl

Master of Science, Metallurgical and Materials Engineering

Supervisor: Prof. Dr. İshak Karakaya

Co-Supervisor: Assist. Prof. Dr. Metehan Erdoğan

July 2020, 81 pages

During the aircraft development process, corrosion acceleration tests are often performed to assess the risk of corrosion of designs when exposed to the outdoor environment for an extended period or to simulate the actual situation the aircraft structure will be exposed to during its life. However, these tests require several months to years to complete. As an alternative approach, computational modeling has the potential to reduce the cost of testing significantly. A calculation model was developed, and experimental validation was performed to simulate galvanic corrosion in the environment to which the aircraft will be exposed to. The numerical approach was based on a 2D boundary/finite element method. The inputs of the problem were the geometric definition and physical properties of the electrolyte and the macroscopic polarization curves of the active electrodes. The main results of the model were corrosion rates, current density, and potential distribution. An experimental setup was established for the validation of the calculation results consisting of a combination of two common planar materials consisting of aluminum AA2024-T3 and carbon fiber reinforced polymer (CFRP). The validation approach is explained, and the critical pit corrosion distance due to galvanic corrosion on the aluminum alloy and the maximum

pit corrosion depth is shown. A reasonably good agreement was reached between the observed and simulated data.

Keywords: Corrosion Modelling, Galvanic Corrosion, Corrosion Risk Assessment, AA2024-T3, CFRP

ÖZ

SAYISAL MODELLEME VE DENEYSEL DEĞERLENDİRME İLE ALÜMİNYUM ALAŞIM AA2024-T3 VE KARBON ELYAF GÜÇLENDİRİLMİŞ PLASTİ ARASINDA GALVANİK KOROZYON TAYİNİ

Yıldırım, Mustafa Anıl
Yüksek Lisans, Metalurji ve Malzeme Mühendisliği
Tez Danışmanı: Prof. Dr. İshak Karakaya
Ortak Tez Danışmanı: Dr. Öğr. Üyesi Metehan Erdoğan

Temmuz 2020, 81 sayfa

Hava aracı geliştirme sürecinde, korozyon tasarımlarının genellikle uzun süre açık hava ortamına maruz kalma riskini değerlendirmek veya hava aracı yapısının ömrü boyunca maruz kalacağı gerçek durumu simüle etmek için korozyon hızlandırma testleri yapılır. Ancak bu testlerin tamamlanması birkaç ay ile yıllarca test süresi gerektirir. Alternatif bir yaklaşım olarak, hesaplama modellemesi, test maliyetini önemli ölçüde azaltma potansiyeline sahiptir. Hava aracının maruz kalacağı çevresel ortamında galvanik korozyonu simüle etmek için bir hesaplama modelinin geliştirilmesi ve deneysel validasyonu yapılmaktadır. Sayısal yaklaşım 2 boyutlu bir Sınır / Sonlu Elemanlar Yöntemi modeline dayanmaktadır. Sorunun girdileri arasında: elektrolitin geometrik tanımı ve fiziksel özellikleri ile aktif elektrotların makroskopik polarizasyon eğrileri bulunmaktadır. Modelin ana sonuçları korozyon oranları, elektrik akım yoğunluğu ve potansiyel dağılımdır. Alüminyum AA2024-T3 ve karbon fiber takviyeli polimerden (CFRP) oluşan ortak düzlemsel iki malzeme kombinasyonundan oluşan hesaplama sonuçlarının validasyonu için bir deney düzeneği oluşturulmuştur. Doğrulama yaklaşımı açıklanmış ve Alüminyum alaşımı üzerinde oluşan galvanik korozyon nedenli kritik çukurcuk korozyonu uzaklığı ve

maksimum oluşabilecek çukurcuk korozyonu derinliği gösterilmiştir. Gözlemlenen ve simüle edilen veriler arasında iyi bir yaklaşım sağlanmıştır.

Anahtar Kelimeler: Korozyon Modellemesi, Galvanik Korozyon, Korozyon Risk Tayini, AA2024-T3, CFRP

To my lovely wife

ACKNOWLEDGEMENTS

I would like to express my deepest gratitude cordially to my supervisor Prof. Dr. İshak Karakaya for his patience, motivation, guidance, advice, criticism, support and insight not only throughout this thesis but in many other studies.

I also wish to express my gratitude to Assist. Prof. Dr. Metehan Erdoğan for his guidance, advice, criticism, support and comments during this study.

I am sincerely grateful to Prof. Dr. Kadri Aydınol, Assist. Prof. Dr. Erkan Konca, and Assist. Prof. Dr. Batur Ercan for their suggestions, comments and support.

I would also like to thank my brother Arda Yıldırım and the members of Thermochemical and Electrochemical Materials Processing Laboratory, especially Esra Sütçü, Çağlar Polat, Olgun Yılmaz and Mustafa Serdal Aras for their support and assistance throughout this thesis.

I must express my very profound gratitude to my love Aslı Gümüş Yıldırım for providing me with unfailing support and continuous encouragement throughout my years of study and through the process of researching and writing this thesis. This accomplishment would not have been possible without her.

And finally, in memory of my dear friend Ece Alpuğan, she brought so many gifts to our life. We will never forget her.

TABLE OF CONTENTS

ABSTRACT.....	v
ÖZ.....	vii
ACKNOWLEDGEMENTS	x
TABLE OF CONTENTS	xi
LIST OF TABLES	xiii
LIST OF FIGURES	xiv
1. INTRODUCTION	1
2. REVIEW OF LITERATURE	7
2.1. Electrochemical Theory [25]	7
2.2. Factors Affecting Galvanic Corrosion.....	14
2.3. Pitting Corrosion on Aluminum [36]	18
3. EXPERIMENTAL METHODOLOGY.....	23
3.1. Potentiodynamic Polarization Resistance Measurement.....	23
3.1.1. Materials	23
3.1.2. Sample Preparation	24
3.1.3. Electrolyte	28
3.1.4. Test Setup	29
3.2. Laboratory Immersion Corrosion Testing	31
3.2.1. Materials	32
3.2.2. Sample Preparation	32
3.2.3. Electrolyte.....	33

3.2.4. Test Setup	33
3.3. Numerical Modelling	35
3.3.1. Setting Model Environment	35
3.3.2. Creating Geometric Object.....	36
3.3.3. Specifying Properties of Materials	37
3.3.4. Defining Physics Boundary Conditions	38
3.3.5. Creating Mesh	45
4. RESULTS AND DISCUSSION	47
4.1. Results of Potentiodynamic Polarization Resistance Measurements.....	47
4.1.1. Critical Pit Current Density	49
4.1.2. Limiting Current Density	50
4.1.3. Mixed Potential Theory	52
4.2. Laboratory Immersion Corrosion Test Results.....	53
4.2.1. Critical Pit Distance.....	53
4.2.2. Maximum Pit Depth	58
4.3. Simulation Results and Validation of Numerical Model	65
4.3.1. Local Current Density	65
4.3.2. Surface Electrolyte Potential	67
5. CONCLUSION	75
REFERENCES	77

LIST OF TABLES

TABLES

Table 3.1. Composition of AA2024-T3 [45].	24
Table 3.2. Electrolyte conductivity and pH measurement.	29
Table 3.3. Potentiodynamic test setup for samples.	31
Table 4.1. The overall Tafel slopes obtained from potentiodynamic tests for AA2024-T3 and CFRP.	49
Table 4.2. Critical pit distance on AA2024-T3 from the joint in microns (The maximum values were shown in Bold).	54
Table 4.3. Maximum pit depth in microns (The maximum values were shown in Bold).	59
Table 4.4. Maximum pit depths result for Godard's model.	64

LIST OF FIGURES

FIGURES

Figure 1.1. Increased use of composite material in Boeing aircraft (The image was reproduced from the source [2]).	2
Figure 1.2. Galvanic corrosion on rivets in the engine area of an aircraft (The image was reproduced from the source [8]).	2
Figure 1.3. Typical example of corrosion type percentage encountered in aircraft parts after almost 40.000 flying hours (The graph was reproduced from the source [8]). ...	3
Figure 2.1. Tafel and linear approximation of Butler Volmer equation (The graph was reproduced from the source [25]).	9
Figure 2.2. Mass transfer effect on Butler-Volmer equation (The graph was reproduced from the source [25]).	11
Figure 2.3. Galvanic couple between two metals (The graph was reproduced from the source [28]).	12
Figure 2.4. Galvanic corrosion impact variables (The diagram was reproduced from the source [31]).	14
Figure 2.5. Galvanic series of some alloys in seawater (The diagram was reproduced from the source [32]).	15
Figure 2.6. Pourbaix diagram of potential-pH for Al-H ₂ O system at 25°C (The diagram was reproduced from the source [38]).	18
Figure 2.7. Pit propagation steps (The diagram was reproduced from the source [43]).	20
Figure 3.1. Potentiodynamic polarization test samples: (a) Main samples tested; (b) Cylindrical sample holder for test setup.	25
Figure 3.2. Potentiodynamic polarization test samples: (a) Test sample with carbon tape; (b) Assembled test sample example; (c) Front view of the assembled test samples.	25

Figure 3.3. Mounting steps: (a) Placing the test sample into the mold; (b) Molding of epoxy cold bakelite; (c) Cooling of liquid epoxy.....	26
Figure 3.4. Grinding steps: (a) Cutting out excess bakelite; (b) Grinding with 1200 and 4000 sandpaper; (c) Front surface view of the sample after sanding; (d) Grinding until to back surface of the sample was opened.	27
Figure 3.5. Continuity control step: (a) Test sample connection step1; (b) Test sample connection step2; (c) Multimeter (Keysight U1282A); (d) Continuity control.	28
Figure 3.6. Possible electrolyte thickness in the aircraft structure [46].	29
Figure 3.7. Potentiodynamic polarization test setup: (a) A schematic test setup and connections (b) Gamry multiport kit with jacketed for electrochemical corrosion cell.	30
Figure 3.8. Immersion corrosion test elements in %5 NaCl solution @RT (a) AA2024-T3; (b) CFRP; (c) RBC coating Titanium bolt.....	32
Figure 3.9. Preparation steps of the test sample (a) Continuity control for CFRP after the glass layer was removed from the surface (b) Combining AA2024-T3 and CFRP material with RBC coating Titanium bolt (c) Final test sample.	33
Figure 3.10. Test setup for corrosion immersion test and electrolyte control mechanism (a) Test samples (b) Test setup (c) Electrolyte level control.	34
Figure 3.11. Selecting physics for modelling (The picture was taken as screenshot from Comsol software).	35
Figure 3.12. Model geometry.....	36
Figure 3.13. Material parameters (The picture was taken as screenshot from Comsol software).....	37
Figure 3.14. <i>Electrolyte conductivity (The picture was taken as screenshot from Comsol software).</i>	37
Figure 3.15. Cathode (CFRP) reaction surface.	38
Figure 3.16. Cathode (CFRP) reaction parameters (The picture was taken as screenshot from Comsol software).	39
Figure 3.17. Anode (AA2024-T3) reaction surface.	40

Figure 3.18. Anode (AA2024-T3) reaction parameters (The picture taken as screenshot from Comsol software).	42
Figure 3.19. Non-Deforming boundaries on model (The picture was taken as screenshot from Comsol software).	43
Figure 3.20. Non-Deforming boundary parameters (The picture was taken as screenshot from Comsol software).	43
Figure 3.21. Deforming electrode surface on model (The picture was taken as screenshot from Comsol software).	44
Figure 3.22. Deforming electrode surface parameters (The picture was taken as screenshot from Comsol software).	44
Figure 3.23. Mesh on model (The picture was taken as screenshot from Comsol software).	45
Figure 3.24. Automatic remeshing option and time dependent study (a)Time dependent parameters; (b) Automatic remeshing option (The picture was taken as screenshot from Comsol software).	46
Figure 4.1. Potentiodynamic polarization measurement for AA2024-T3.	47
Figure 4.2. Potentiodynamic polarization measurement for CFRP.	48
Figure 4.3. AA2024-T3 Potentiodynamic polarization critical current.	49
Figure 4.4. Example of stable and metastable pitting potential curve of a passive metal (The graph is reproduced from the source [52])	50
Figure 4.5. Potentiodynamic polarization curves for mixed AA2024-T3 and CFRP.	52
Figure 4.6. The region where the galvanic corrosion effect was examined on the aluminum AA2024-T3.....	53
Figure 4.7. Maximum critical pit distance sample 2 after 3 days immersion test.	55
Figure 4.8. Maximum critical pit distance sample 4 after 15 days immersion test. ..	55
Figure 4.9. Maximum critical pit distance sample 7 after 45 days immersion test. ..	56
Figure 4.10. A typical SEM (Scanning electron microscope) image of joint area of test sample 2 subjected to immersion test for 3 days.	57
Figure 4.11. Elemental mapping analysis of joint area.	57

Figure 4.12. Quantitative elemental analysis of joint area	58
Figure 4.13. Sample preparation steps to measure maximum pit depth (a) Cutting step; (b) Cross-section sample; (c) Conductive bakelite step.	59
Figure 4.14. Maximum pit depth of sample 2 after 3 days immersion test.	60
Figure 4.15. Maximum pit depth of sample 5 after 15 days immersion test.	61
Figure 4.16. Maximum pit depth of sample 7 after 45 days immersion test.	62
Figure 4.17. Pit shape standards according to ASTM G-46 [55].....	62
Figure 4.18. Godard's model relationship between maximum pit depth and exposure time [56].....	63
Figure 4.19. Fitting experimental data to the kinetic model.	64
Figure 4.20. Elemental mapping analysis of pit depth area.	65
Figure 4.21. Local corrosion current density distribution on 2024-T3 and CFRP surfaces distribution calculated by using Comsol Multiphysics software.	66
Figure 4.22. Local corrosion current density distribution on 2024-T3 and CFRP surfaces distribution in zoom view with stable and metastable region. Point A (4500 microns), Point B (6000 microns), and Point C (7900 microns) represent the critical pit distances from the joint for 3, 15, and 45 days respectively	67
Figure 4.23. Surface electrolyte potential distribution at T=45 Days.	68
Figure 4.24. Deformation on AA2024-T3 boundary and surface electrolyte potential distribution at T=0 Days.	69
Figure 4.25. Deformation on AA2024-T3 boundary and surface electrolyte potential distribution at T=3 Days.	69
Figure 4.26. Deformation on AA2024-T3 boundary and surface electrolyte potential distribution at T=15 Days.	70
Figure 4.27. Deformation on AA2024-T3 boundary and surface electrolyte potential distribution at T=45 Days.	70
Figure 4.28. Comparison of critical pit distance results between modelling (shown with line) and immersion test (shown with bars).	71
Figure 4.29. Comparison of maximum pit depth results between modelling (shown with line) and immersion test (shown with bars).	72

Figure 4.30. Convergence of modeling to experimental values.	73
---	----

CHAPTER 1

INTRODUCTION

In today's aviation industry, the design of the aircraft by reducing the weight of aircraft is becoming more and more critical because it is intended to minimize the impact of the aviation industry on global warming and environmental pollution, and at the same time, produce more fuel-saving aircraft [1]. For example, on a Boeing 787, 10% -12% savings in fuel consumption was achieved with 20% weight reduction [2]. In expansion to the diminishment of carbon footprint, weight-reducing aircraft designs have also achieved results that increase flight performance, such as faster take-off, and higher structural strength [3]. The fundamental guideline of lightweight plans is to decrease the fabric utilized or to utilize materials with lower thickness and at the same time, not losing any of its performance [4].

The selection of aviation materials covers the period from the design stage to the end of the life of the materials and is very important for many reasons. A structural aerospace material must meet the requirements in low density; high corrosion resistance. Also, cost, service, and manufacturability characteristics should be high [5].

To meet the demand for high fuel efficiency in aircraft and to increase the life and overall performance of structures, complex combinations of light materials such as aluminum, magnesium, titanium, and CFRP are continually being developed and used by the aircraft industry [6]. As an example shown in Figure 1.1 for Boeing commercial passenger planes.

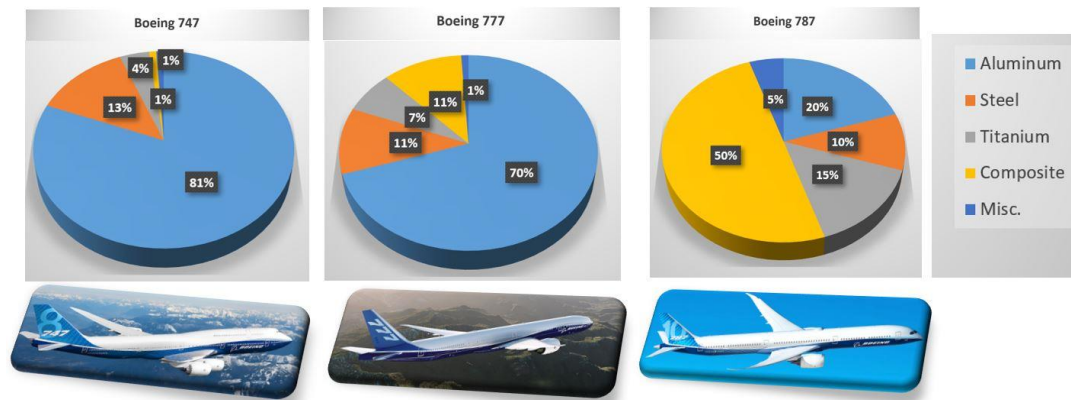


Figure 1.1. Increased use of composite material in Boeing aircraft (The image was reproduced from the source [2]).

However, in the presence of a conductive electrolyte due to the environmental impacts of the aircraft during use, the combination of such different materials can lead to accelerated galvanic corrosion, which can pose serious structural problems to the plane if adequate corrosion control measurement is not taken into account [7]. For example, galvanic corrosion on rivets in the engine area of an aircraft is shown in Figure 1.2.

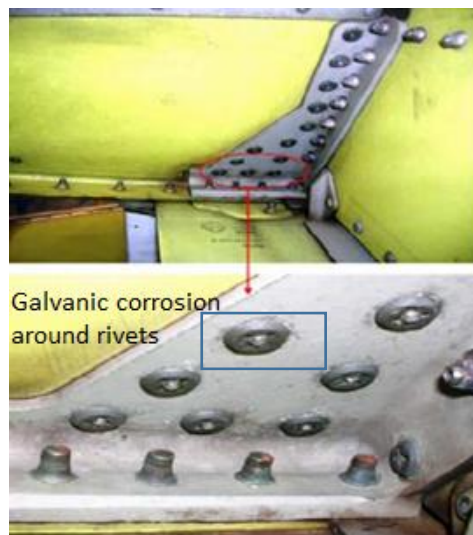


Figure 1.2. Galvanic corrosion on rivets in the engine area of an aircraft (The image was reproduced from the source [8]).

Galvanic corrosion is the typical form of corrosion that occurs when two materials with different electrochemical properties are combined in the presence of an abrasive electrolyte, causing the breakdown of the more electrochemically anodic component [9]. For example, galvanic corrosion is the primary corrosion mechanism of the corrosion damage cases of the aircraft structure [8] encountered in different part of typical passenger plane have found corrosion type percentage as shown in Figure 1.3. Therefore, protection against galvanic corrosion plays a vital part within the plan and support techniques of airplane [10].

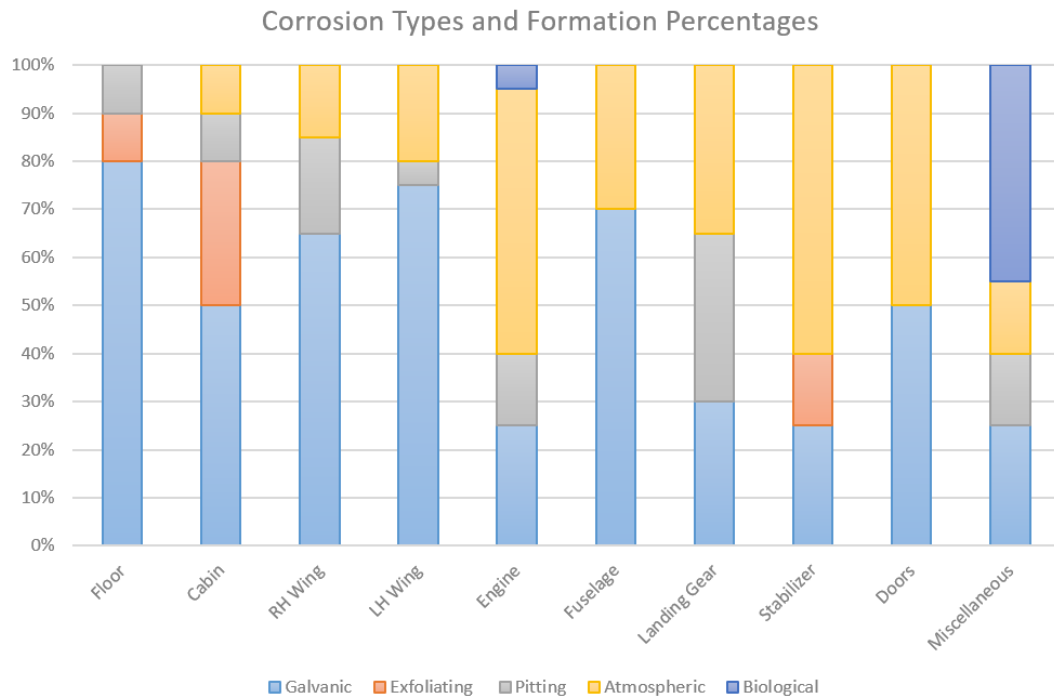


Figure 1.3. Typical example of corrosion type percentage encountered in aircraft parts after almost 40.000 flying hours (The graph was reproduced from the source [8]).

The “find and correct” maintenance concept currently applied in the aerospace industry is a common approach to corrosion that needs to be repaired and maintained without affecting the operational effectiveness of the corrosion damage. However, it is widely accepted that planned maintenance measures are more efficient in the medium to long term, so the benefit of modeling becomes clear for the prediction of corrosion risk and optimum design. The “find and correct” approach should be complemented by an understanding of the corrosion process and the ability to predict its behavior. The use of corrosion prediction models can lead to the development of cost-effective predictive corrosion integrity and maintenance programs [10].

The fundamental standards of galvanic corrosion are well characterized and well caught on. Still, the general understanding so far has not yet been sufficiently used to narrow the gap between scientific research and reality. On the other hand, the advance of computational assets over the past few decades has presently made it possible to model various complex corrosion systems, thus representing a pioneering technology not only for research in the field but also for direct application in engineering design [11]. Currently, a computational modeling approach is one of the foremost viable apparatuses for plan and optimization, as well as blunder discovery, observing, and quality execution assessment. One of the general objectives of modeling galvanic corrosion is to adjust corrosion security measures to prevent galvanic corrosion for hybrid structures without performing multiple laboratory tests. An important viewpoint of computational modeling for galvanic corrosion is its pertinence to reality and its unwavering quality as a prescient apparatus. In this manner, the confirmation step of any demonstration is as imperative as the other perspectives of the exhibit [12].

This ponder for the most part depicts the advancement of a conceptual galvanic corrosion model based on the Boundary / Finite Element Method to optimize the protection of galvanized corrosion from mixed structures under electrolyte layers in aircraft structures [13].

Galvanic corrosion modeling has proven its applicability among corrosion modeling studies [14–17]. Deshpande [18] reported that galvanic corrosion couple rates can be well predicted that magnesium alloy AE44–mild steel couple and AE44–aluminium alloy AA6063 couple in brine solution were studied by Comsol software and model was validated with both immersion test and Scanning Vibrating Electrode Technique (SVET). Y.Zhang et al. [19] presented galvanic corrosion of aluminum alloy in single bolted lap joint (both bare and coated) in an aircraft structure simulated in atmospheric condition by using thin film approach. They proved their modelling studies with potential and current measurement on the anode surface. Some studies focuses on the coating application, Samuel R. Cross et al. [20] developed numerical modelling for galvanic corrosion of zinc and aluminum coating which were galvanically coupled to a mild steel substrate in H_2SO_4 electrolyte. Simulation was validated with corrosion testing and electrochemical measurement.

Only few works presented galvanic corrosion modelling, especially between aluminum alloy and CFRP [21–23]. Among these studies, S. Palani et al. [23] investigated and validated atmospheric corrosion on AA2024-T3 and CFRP couple with very thin electrolyte of different thickness (13 μm - 45 μm). The outcomes of this modelling were electric current density and potential distribution on the electrode surface. As a result of modeling, potential, and current changes on the surface with very thin electrode thicknesses were validated with real-time electrochemical measurements. M. Mandel and L. Krüger [22] developed the galvanic corrosion model between aluminum alloy AA6060-T6 and CFRP, and validated this model by immersion test that showed critical pitting sensitivity on the aluminum alloys, which provides a link between galvanic corrosion induced pitting corrosion, has been associated and a critical pitting corrosion distance has been defined.

Within the scope of this work, it has been aimed to contribute to the literature by modeling the pitting corrosion sensitivity and critical pitting corrosion distance and determining the critical pitting corrosion distance for the aluminum AA2024-T3 and CFRP galvanic pair, which have not been studied before, and to validate the results by immersion tests for 3, 15 and 45 days. The validation approach involves comparing the experimental measurements of electrolyte potential and corrosion rates from an abrasive sample with estimates from the equivalent calculation model. The materials included in the experiment are bare aluminum alloy AA2024-T3 and CFRP, which serve as anode and cathode, respectively.

CHAPTER 2

REVIEW OF LITERATURE

Galvanic corrosion is simply a type of corrosion that occurs when a metal comes into contact with another conductive material in a conductive and corrosive environment. The driving force of the process is the electrochemical potential differences between the two materials in contact. The relatively noble material acts as a cathode, that is, where some oxidizing species are reduced, and the more active material is the anode, where corrosion occurs. The metal dissolves in the anodic reaction, oxygen reduction or hydrogen evolution in the cathodic reaction, or both [24].

2.1. Electrochemical Theory [25]

Thermodynamics of Electrode Reactions

Under equilibrium conditions, the reaction of a simple electrode can be defined as:



Where O represents oxidized species, R is the reduced species, and n is the number of electrons in the reaction.

The standard potential of the reaction is that under standard conditions, considering the electrolyte solution and the activity of all ions in the reactions as unity and the pressure of the gas as 1 atm [26]:

$$E^0 = -\Delta G^0/nF \quad (2)$$

Where ΔG^0 is the standard Gibbs free energy of the reaction.

The electrode potential of the reaction under the non-standard condition is represented by:

$$E = E^0 - \frac{RT}{nF} \ln \frac{C(R)}{C(O)} \quad (3)$$

Where $C(R)$ and $C(O)$ show the activities of the reduced and oxidized species for above reduction process. This equation is also known as the Nernst equation. It identifies potential deviations in the electrode reaction under equilibrium conditions.

Kinetics of Electrode Reactions

While the reaction takes place in nonequilibrium conditions, two opposite currents densities, one anodic $i(a)$ and one cathodic $i(c)$ and net current density i are formed. Therefore:

$$i = i(c) - i(a) \quad (4)$$

At equilibrium condition, no net current density formed

$$i_0 = i(c) = i(a) \quad (5)$$

Where i_0 represent the exchange current density

The relationship between current and potential for reaction 1 can be explained by the following equation as well known Butler-Volmer equation by neglecting the mass transfer effect.

$$i = i_0 \left[\exp \left(-\frac{\alpha n F \eta}{RT} \right) - \exp \left(\frac{(1 - \alpha) n F \eta}{RT} \right) \right] \quad (6)$$

i is the current density

i_0 is the exchange current density

α is the transfer coefficient

η is the overvoltage

Exchange current density is given by:

$$i_0 = nFk_0C(O)_s^\alpha C(R)_s^{1-\alpha} \quad (7)$$

Where $C(O)_s$ and $C(R)_s$ show the activities of oxidized and reduced species at the electrode surface at equilibrium.

Where k_0 is the reaction rate constant

The relationship of Butler Volmer equation with Tafel and linear approximation method shown in Figure 2.1 below as i/i_0 counter $\alpha nF\eta/RT$

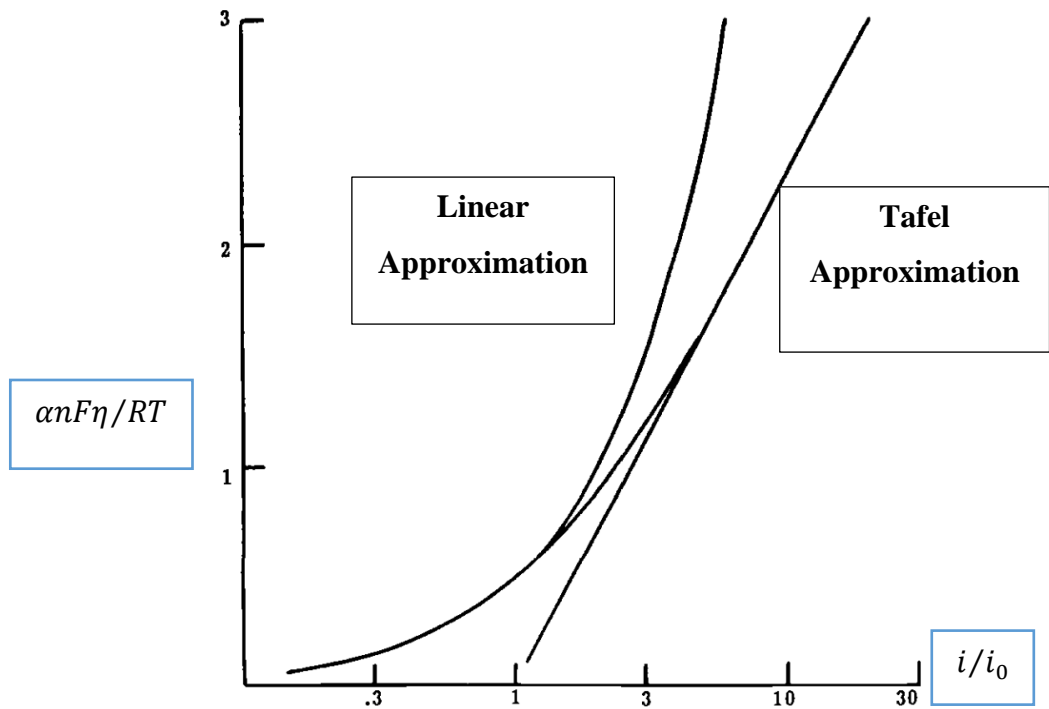


Figure 2.1. Tafel and linear approximation of Butler Volmer equation (The graph was reproduced from the source [25]).

Reverse voltage reaction value can be neglected at high voltage values. In this way, the equation (6) becomes the known Tafel equation:

$$\log i = \log i_0 + \frac{\alpha n F \eta}{2.3 RT} \quad (8)$$

Linear expansion of exponential terms at low voltage values $2\alpha = 1$ considering the following decimal.

$$i = i_0 \frac{n F \eta}{RT} \quad (9)$$

When the mass transfer effect is added to Equation (6) [27].

$$i = i_0 \left[\frac{i_1(a)}{i_1(a) - 1} \exp \left(-\frac{\alpha n F \eta}{RT} \right) - \frac{i_1(c)}{i_1(c) - 1} \exp \left(\frac{(1 - \alpha) n F \eta}{RT} \right) \right] \quad (10)$$

Where $i_1(a)$ and $i_1(c)$ are the anodic and cathodic diffusion limited current densities represented by:

$$i_1(a) = \frac{n F D(R)}{\delta} (C(R)_B - C(R)_S) \quad (11)$$

and

$$i_1(c) = \frac{n F D(O)}{\delta} (C(O)_B - C(O)_S) \quad (12)$$

$D(R)$ and $D(O)$ are the diffusion coefficients of reduced and oxidizing species, respectively, and δ is the thickness of the diffusion layer. Subscript B represents bulk concentrations

At high overvoltages, equation (10) can be simplified by neglecting back reaction. An example cathodic reaction can be shown as the equation below.

$$i = \frac{i_0 \exp \left(-\frac{\alpha n F \eta}{RT} \right)}{1 + \frac{i_0}{i_1(a)} \exp \left(-\frac{\alpha n F \eta}{RT} \right)} \quad (13)$$

With the mass transfer effect, a comparison between equations (13) and (8) can be seen on Figure 2.2 graphically.

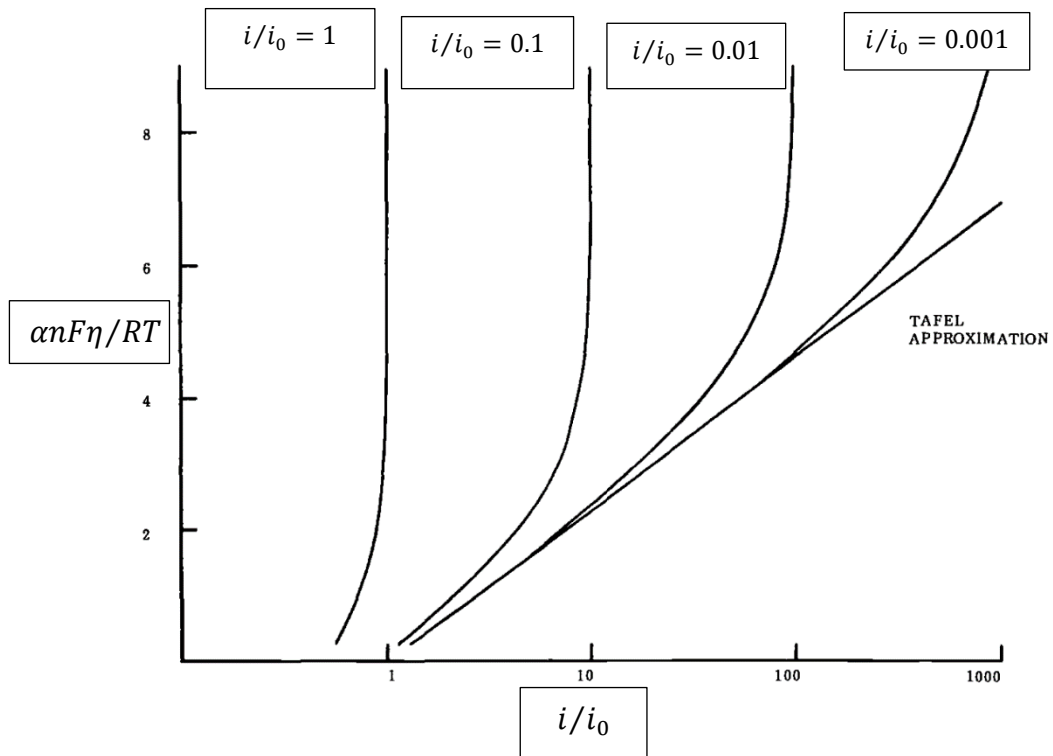


Figure 2.2. Mass transfer effect on Butler-Volmer equation (The graph was reproduced from the source [25]).

In general, Equations (6) and (10) versions serve as general expressions for an electrode reaction rate in terms of reaction rate constant, the concentration of reacting species, and electrode overvoltage.

Mixed Potential Theory on Two Materials

The mixed potential theory can be explained by combined electrodes on which two or more oxidation and reduction reactions occur. This indicates that two or more electrochemical reactions can occur simultaneously on the surface of a metal in a solution or similar metals. The total potential resulting from the corrosion process is defined as mixed or corrosion potential and explains that when the sum of the whole anodic currents and total cathodic currents is equal at this potential, the net current or current density is zero [28]. The protection of the load is balanced by the net reaction rates of the anode and cathode. In Figure 2.3, electrochemical reactions of abrasive metals M_1 and M_2 , when combined in the same solution, are represented in a graphical form called the Evans diagram.

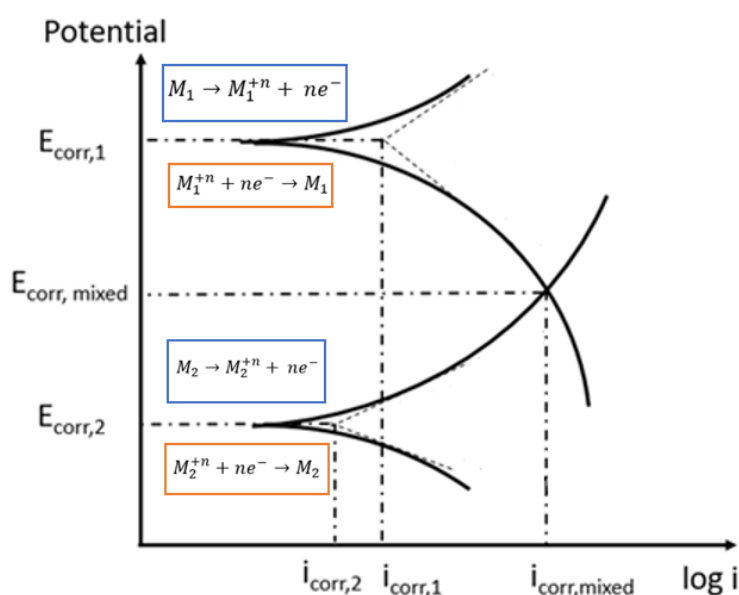


Figure 2.3. Galvanic couple between two metals (The graph was reproduced from the source [28]).

According to Wagner and Traud [29], the intersection point obtained by extrapolation of both anodic and cathodic partial polarization curves gives the corrosion potential and corrosion current density of the total reaction.

Laplace's and Poisson's Equations

The corrosion rate at any point on a metal surface in an electrolyte can be estimated if the electrochemical potential in the electrolyte adjacent to that point is known. The equation regulates the distribution of potential in a galvanic system [30].

Charge conservation requires that the current per unit volume / relates to the charge density q by

$$-\nabla \cdot i = \frac{\delta q}{\delta t} \quad (14)$$

Where $\nabla = (\delta/\delta x) + (\delta/\delta y) + (\delta/\delta z)$

For a steady state $\delta q/\delta t = 0$

With the relationship for electric field intensity

$$E = -\nabla \phi \quad (15)$$

By applying Ohm's law;

$$i = \sigma E \quad (16)$$

The continuity equation transformed to

$$\nabla \phi \nabla \sigma = 0 \quad (17)$$

For uniform, isotropic conductivity, Laplace equation can be achieved.

$$\nabla^2 \phi = 0 \quad (18)$$

This continuity equation becomes the Poisson equation at the points where the polarization currents i_p in the electrolyte enter or exit.

$$\nabla \phi \nabla \sigma + i_p = 0 \quad (19)$$

The solution of this equation with appropriate anodic and cathodic polarization expressions and related boundary conditions will give the potential distribution throughout the electrolyte and thus the corrosion rates on the component metals in the system.

2.2. Factors Affecting Galvanic Corrosion

Apart from electrochemical effects, many factors are affecting galvanic corrosion. The factors that are summarized are shown in Figure 2.4. A summary on the effects of each factor is given below.

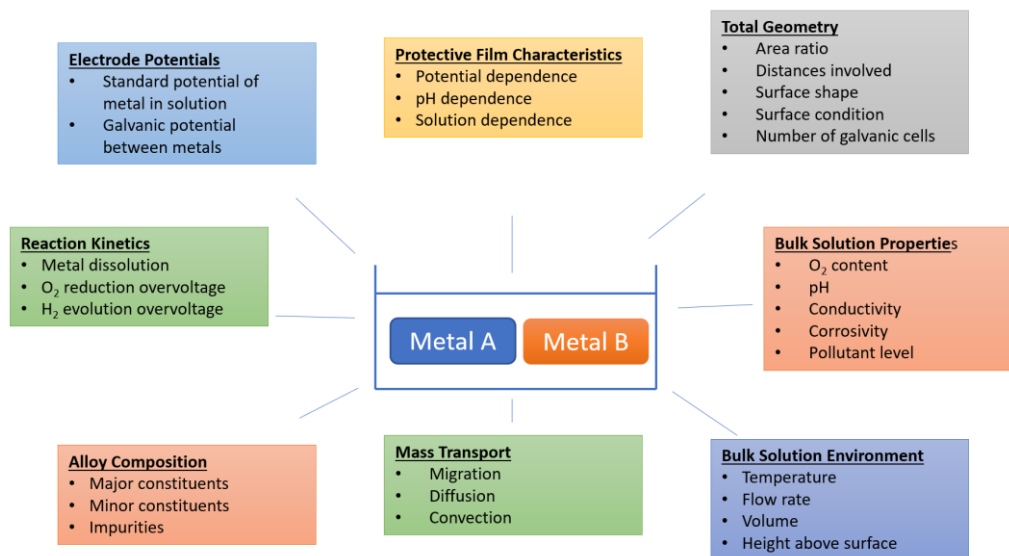


Figure 2.4. Galvanic corrosion impact variables (The diagram was reproduced from the source [31]).

Electrode Potentials

The standard electrode potential of a metal in a solution of its ions gives a rough guide to the position of that metal in the galvanic series. In practice, the best method of obtaining a "galvanic series" of potentials, some of them, according to relative positions, are shown in Figure 2.5, is to measure these potentials in the environment under consideration.

Reaction Kinetics

Electrode potential data will show whether galvanic corrosion will occur. Reaction kinetic data shows how fast corrosion can occur. Metal dissolution kinetics provide information about the rate of anodic reaction in the corrosion cell; oxygen depletion or hydrogen development overvoltage on both metals or alloys, or both rate of cathodic reactions and whether they will occur on one or both materials.

Alloy Composition

The composition of an alloy directly affects the corrosion resistance of the alloy, affecting galvanic corrosion. Also, the components affect the corrosion potential and the kinetics of the related cathodic processes; small components and impurities can play an essential role in this regard.

Protective Film Characteristics

The properties of the protective film, found in most metals and alloys, are important in determining whether galvanic corrosion will occur and what form it will take, for example, in a specific environment, either general or locally. Potential dependence, pH dependence, and resistance to various solution components are particularly important.

Total Geometry

One of the most critical parameters in galvanic corrosion is the "area ratio," high cathode/anode ratio, or high anode/cathode ratio giving slow corrosion or high corrosion, resulting in rapid corrosion. When choosing materials to be used in material design, if it is inevitable to use galvanically incompatible materials, the surface area of the material that will act as an anode should be more than the other material.

Modelling Galvanic Corrosion

Galvanic series, as shown in Figure 2.5, have been used as a guide on whether galvanic corrosion will occur for many years. Qualitative statements about the possible degree of attack are often related to the series. Such tables and guides are useful, but they do not make a quantitative assessment of the degree of corrosion or from which area to expect. This can only be done with detailed and time-consuming tests in the appropriate environment, or with some form of mathematical modeling [33].

The electrochemical reactions involved in galvanic corrosion, in mathematical terms, have pointed out that Laplace's and Poisson's equations must be solved with the relevant boundary conditions to give the current and potential distribution of the system [34]. The advantages of analytical techniques are that they offer a precise solution based on the assumptions made. Although serial solutions based on simple geometries and boundaries are instructive, they are not in actual practical use. The finite difference technique can be used for slightly more complex situations. Although they are assumed to provide analytical solutions, the relevant geometries are still relatively simple. The finite element approach, on the other hand, complex geometry and polarization relations. Finite difference and accuracy of the results obtained using finite element techniques it is largely determined by the available computer capacity. This determines the number of "differences" and "elements", respectively, that can be addressed [35].

2.3. Pitting Corrosion on Aluminum [36]

Aluminum and its alloys are thermodynamically active metal, and it is resistant against corrosion with the protective oxide film it forms on it. When looking at the Pourbaix diagram in Figure 2.6, which contains the potential-pH diagram to see the behavior of the aluminum in aqueous solutions at room temperature, it is seen in which thermodynamic conditions passive protective film layer is formed. As it is understood from the diagram, aluminum between 4-9 pH range forms passive film for 10^{-6} molar soluble species. The thickness of the protective passive oxide film formed in the aqueous environment and at room temperature consists of several nanometers and shows an amorphous structure. As the ambient temperature increases, a thicker film layer is formed [37].

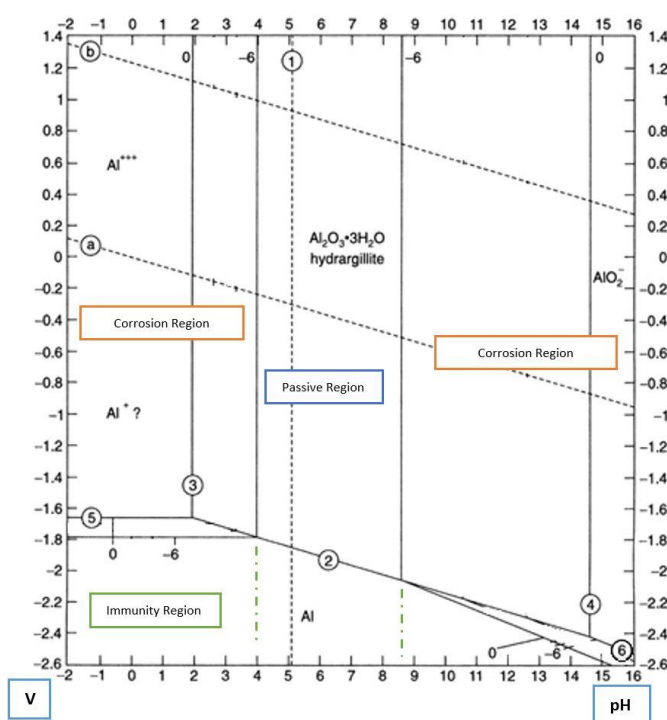
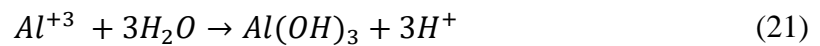


Figure 2.6. Pourbaix diagram of potential-pH for Al-H₂O system at 25°C (The diagram was reproduced from the source [38]).

In aluminum alloys exposed to inorganic salt solutions with a pH of 5-8.5, local pitting corrosion is observed rather than homogeneous corrosion. It has been observed that pitting corrosion formation in solutions containing chloride ions is much more than other solutions. The rate of corrosion formation depends on the specific amount of ions present in the solution. Generally, the corrosion rate in acid solutions containing chloride is very high, and it is harmful to the material [39].

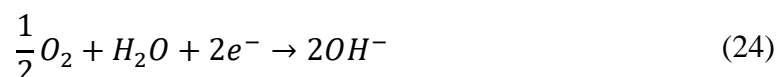
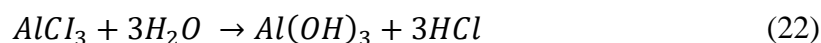
The corrosion product aluminum hydroxide formed in the pitting corrosion seen in aluminum and its alloys is generally small, white and covers the pitting formed [40]. When exposed to an environment outside the pH range where aluminum and its alloys do not form the natural protective oxide layer, homogeneous corrosion attacks begin. When the potential in the environment reaches the potential value required for pitting corrosion, pitting corrosion occurs. Pitting corrosion starts at the weakest point of the passive layer on the surface of the aluminum alloy [41].

Reactions on the anode:



The pH value becomes more acidic when the hydroxide ions are consumed by the migration of chloride ions during the anodic reaction. These ions assist in the formation of anodic reaction and give the formation of aluminum chloride compound and hydroxide and acid by hydrolysis. For this reason, pH values approach acidic values.

Reactions on the cathode:



It is more alkaline due to the formation of hydroxide in the cathode reaction. Oxygen in the environment is a significant factor in the formation of pitting corrosion.

Pitting Corrosion Steps

The start of the pitting corrosion of the aluminum in an oxygenated chloride solution controls the kinetics of the cathodic reaction [42]. A sufficient amount of chloride ion concentration is required in the pit formed for pitting corrosion to progress. These chloride ions cause the formation of $AlCl_3$ compound in the active pit as shown in Figure 2.7.

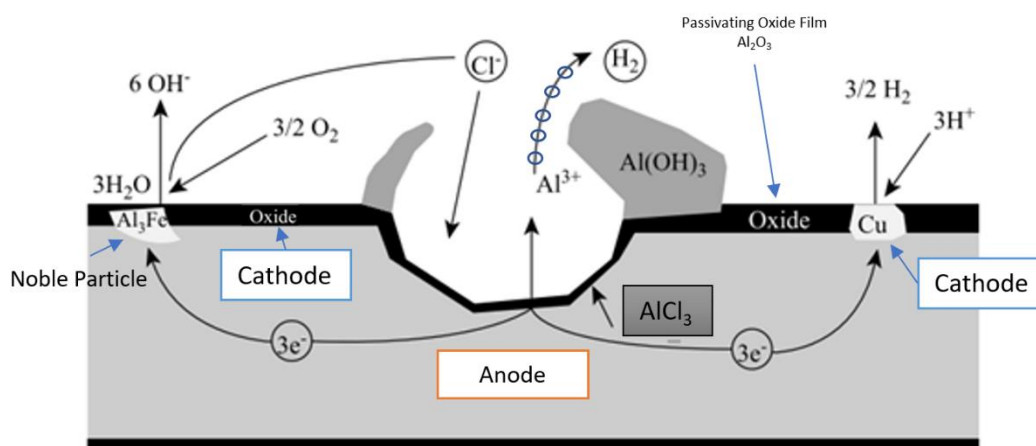


Figure 2.7. Pit propagation steps (The diagram was reproduced from the source [43]).

Reboul et al [43] described the pitting corrosion mechanism and its progress on aluminum in steps below.

- Chlorine ions leak into the passive film with the help of a high electric field into the oxide film layer on the material through micro flaws and locally creates an aluminum-air corrosion cell.
- Slow start of oxygen reduction reaction in the cathodic region.
- Oxide film breakage from a weak point due to micro-cracks.
- Initiation of rapid aluminum oxidation and formation of soluble chloride and oxychloride compounds at the bottom of micro cracks.
- Hydrolysis of soluble chlorides/oxychlorides increases the acid levels of the pit in the exposed solution.
- Due to the continuation of the reactions formed, the accumulation of cone-shaped corrosion products in the mouths of the pits occurs by dissolving hydroxide compounds in the pits and the precipitation of aluminum hydroxide outside the pits.
- Due to the formation of aggressive hydrochloric acid, aluminum corrosion continues in the bottom of the pit.
- Over the time, the chloride/oxychloride film is dissolved and replaced with a passive oxide film, thereby halting the pitting corrosion.

CHAPTER 3

EXPERIMENTAL METHODOLOGY

3.1. Potentiodynamic Polarization Resistance Measurement

It is associated with the potential applied externally to a material in the electrolyte desired to be tested, causing reactions to start at the anode and cathode. Electrochemical information can be obtained over the system to which potential dynamic measurement scanning was applied. This technique can provide information about the corrosion rate, the kinetic data of the pitting corrosion and passivation formations such as passivity region and activity region potential ranges, as well as the cathodic behavior of the material [44].

3.1.1. Materials

Corrosion behavior of aluminum alloy AA2024-T3 (SAE AMS QQ-A-250/5) clad sheet and CFRP (Carbon-fiber-reinforced plastic) epoxy prepreg 120°C cure materials were investigated separately by potentiodynamic polarization resistance measurements. The T3 temper designation of the aluminum alloy means solution heat-treated, cold worked, and naturally aged. The chemical composition of aluminum alloy AA2024-T3 is given in Table 3.1.

Table 3.1. *Composition of AA2024-T3* [45].

<i>Element</i>	<i>Weight %</i>
Copper (Cu)	3.80 - 4.90
Magnesium (Mg)	1.20 - 1.80
Manganese (Mn)	0.30 - 0.90
Silicon (Si)	Max. 0.50
Iron (Fe)	Max. 0.50
Zinc (Zn)	Max. 0.25
Titanium + Zirconium	Max. 0.20
Titanium	Max. 0.15
Chromium (Cr)	Max. 0.10
Other (Each)	Max. 0.05
Others (Total)	Max. 0.15
Aluminum (Al)	Balance

3.1.2. Sample Preparation

The samples used in the potentiodynamic polarization test setup system are normally cylindrical and attached to the test setup with a screw. Since CFRP cannot be found as a rod, it was integrated to the system with the help of a cylindrical sample holder (see Figure 3.1b). Flat test samples were sequentially cut to 10x10 mm squares and attached to the cylindrical sample holder by a carbon tape (see Figure 3.2.) Then, they were taken to cold mounting; the surface was cleaned with sandpaper and finally mounted on the system to check the electrical conductivity.

Cutting

AA2024-T3 and CFRP plate samples that were subjected to the potentiodynamic polarization tests were cut by an ATM Brillant 220 precision cutting device, in the form of 10x10 mm squares as seen in Figure 3.1a. To allow the samples to be suitable for the test setup, the cylindrical sample holder, made of aluminum as shown in Figure 3.1b.

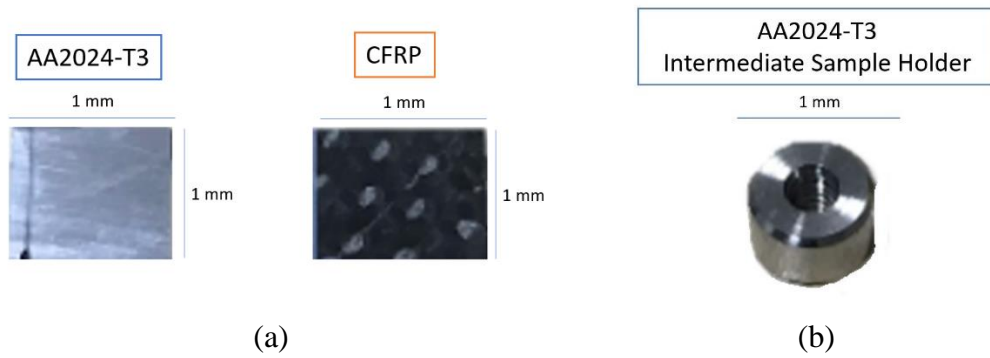


Figure 3.1. Potentiodynamic polarization test samples: (a) Main samples tested; (b) Cylindrical sample holder for test setup.

Assembly

To integrate the flat test samples to the test system, the material to be tested was bonded to the previously cut cylindrical sample holder with the help of a carbon tape. In this way, the flat sample was connected to the system both physically and electrically as seen in Figure 3.2.

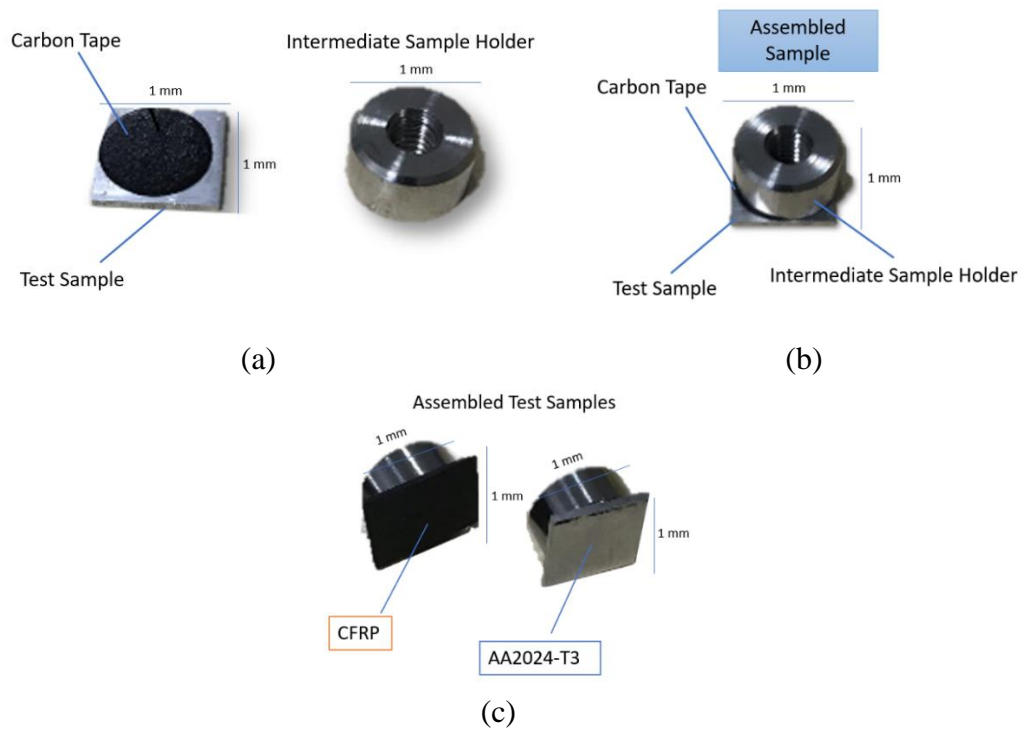


Figure 3.2. Potentiodynamic polarization test samples: (a) Test sample with carbon tape; (b) Assembled test sample example; (c) Front view of the assembled test samples.

Mounting

For the potentiodynamic polarization tests to be carried out properly, only the 10x10mm test specimen should come in contact with the electrolyte. To ensure this, epoxy cold embedding was applied to the assembled test samples as shown in Figure 3.3. The insulating tape was glued to prevent the epoxy from entering the hole portion of the sample. After the epoxy was poured on to the samples, it was left to solidify for about 15-20 minutes. After solidification, the samples were removed from the mold.

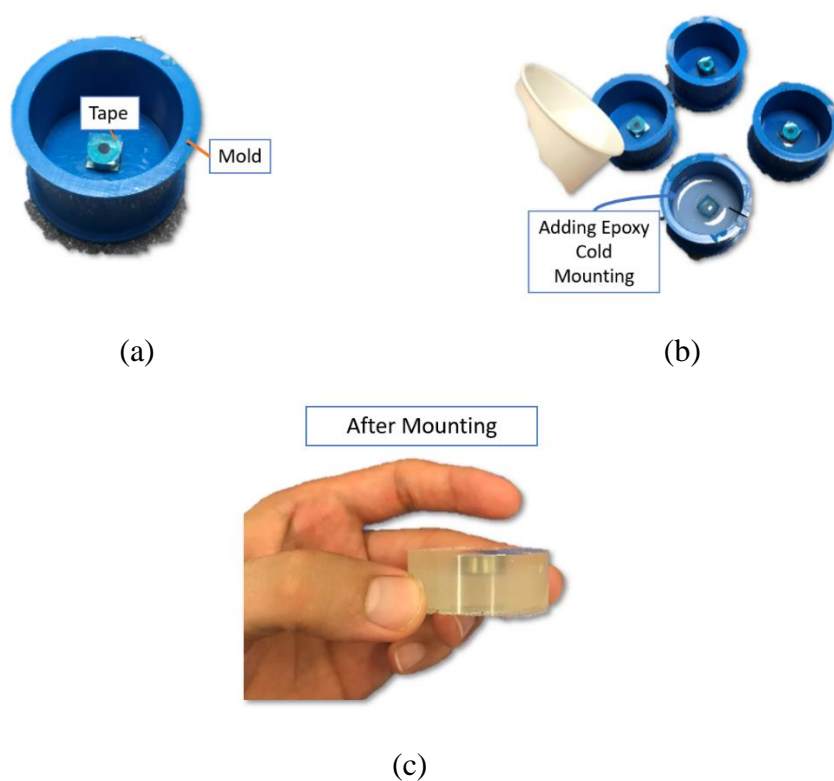


Figure 3.3. Mounting steps: (a) Placing the test sample into the mold; (b) Molding of epoxy cold bakelite; (c) Cooling of liquid epoxy.

Grinding

Since the backside of the test specimen remained in bakelite after cold molding, the excess area was cut with the precision cutting device as shown in Figure 3.4a. The front of the test specimen was then sanded with SiC foil #1200-4000 (see Figure 3.4b

and Figure 3.4c). The back of the sample was sanded until the surface was opened by using Struers Tegramin-25 Grinding and Polishing Equipment (see Figure 3.4d).

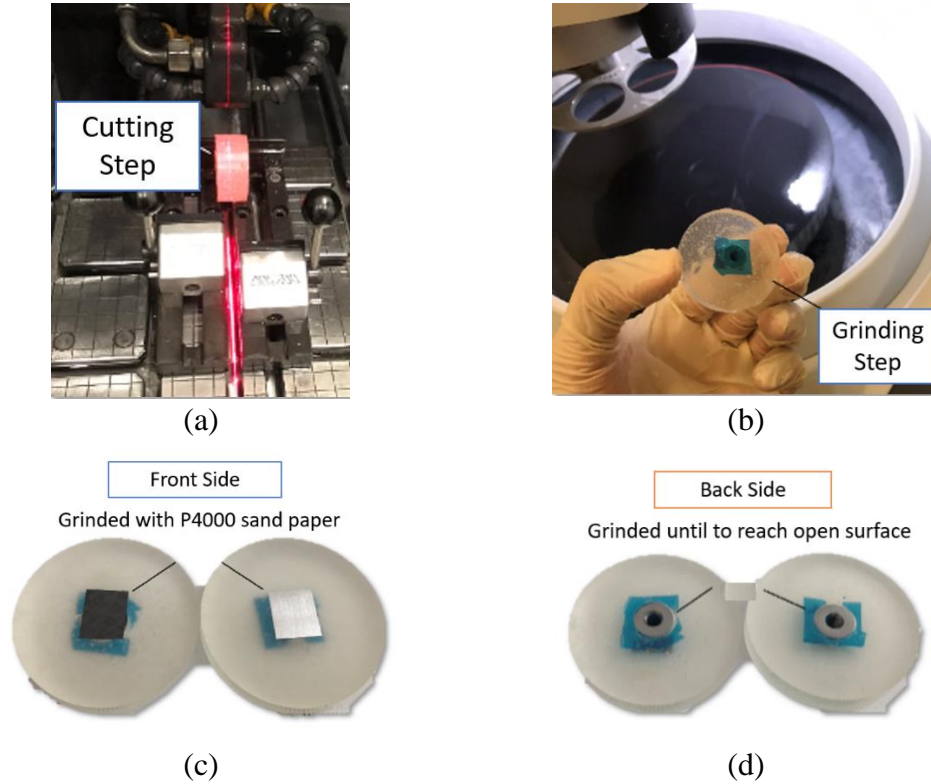


Figure 3.4. Grinding steps: (a) Cutting out excess bakelite; (b) Grinding with 1200 and 4000 sandpaper; (c) Front surface view of the sample after sanding; (d) Grinding until to back surface of the sample was opened.

Continuity Control

The test samples were finally mounted to the gears of the cylinder sample, as shown in the Figure 3.5a on the Gamry test assembly. As shown in Figure 3.5b, the joint was protected from liquid contact using a Teflon apparatus and tape to ensure the insulation. The continuity of the aluminum and carbon fiber test specimen setups were then checked using a multimeter. As shown in Figure 3.5c and Figure 3.5d, one end of the multimeter was contacted to the front of the test specimen, and the other end to the conductor and the continuity of the system was tested ($<30.0\text{k}\Omega$).

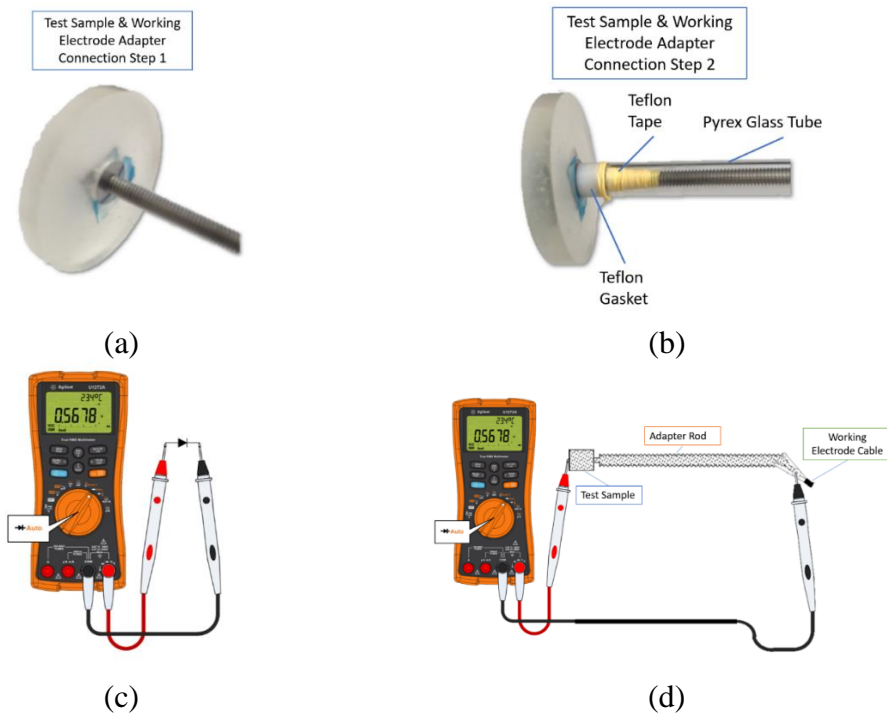


Figure 3.5. Continuity control step: (a) Test sample connection step1; (b) Test sample connection step2; (c) Multimeter (Keysight U1282A); (d) Continuity control.

3.1.3. Electrolyte

Figure 3.6 shows the possible corrosive environments that may occur in a typical aircraft structure while in service [46]. While the corrosive environment on the upper part of the aircraft frame contains a thin layer and low conductivity, the thickness of the corrosive electrolyte increases, and the conductivity increases as it goes down. Therefore, the most aggressive effect of corrosion appears in the lower parts of the aircraft frame. To represent this condition, 5 wt.% NaCl solution was used in both electrochemical measurement and immersion testing [47].

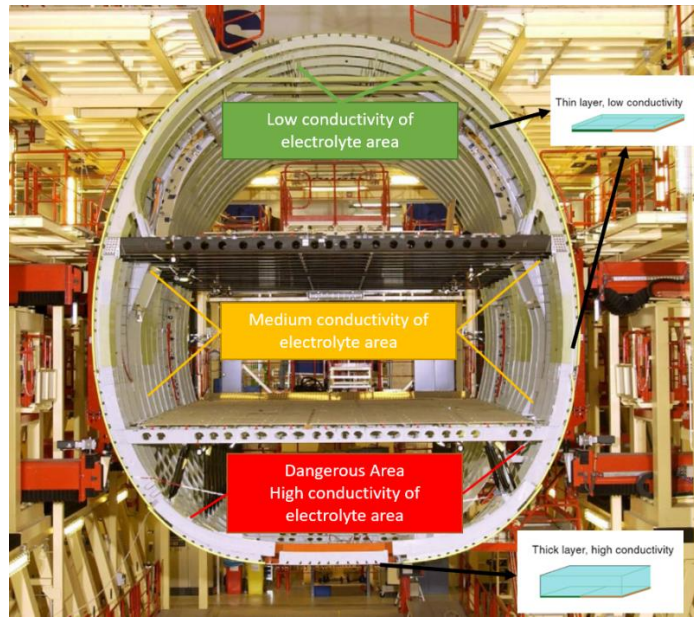


Figure 3.6. Possible electrolyte thickness in the aircraft structure [46].

Then, conductivity and pH measurement were performed for numerical modelling input by using Thermo Scientific Orion Star A211 pH Benchtop Meter. The results are shown in the Table 3.2.

Table 3.2. *Electrolyte conductivity and pH measurement.*

<i>Composition (%wt)</i>	<i>pH</i>	<i>Conductivity (mS/cm)</i>
5 wt.% NaCl solution	5.7	≈83

3.1.4. Test Setup

The potentiodynamic polarization scanning experimental setups were prepared for AA2024-T3 and CFRP materials separately. The tests were carried out in a specially produced glass made Gamry jacketed multiport kit. Electrolyte (%5 NaCl solution) was added to the corrosion cell. The materials were mounted on the working electrode part as the sample to be measured. The counter electrode was graphite and saturated calomel electrode (SCE) was placed as the reference electrode. The cables of all electrodes were then connected to the GAMRY REFERENCE 600 instrument. The

data generated after scanning was analyzed by Gamry Frame Work software installed on the computer as seen in Figure 3.7.

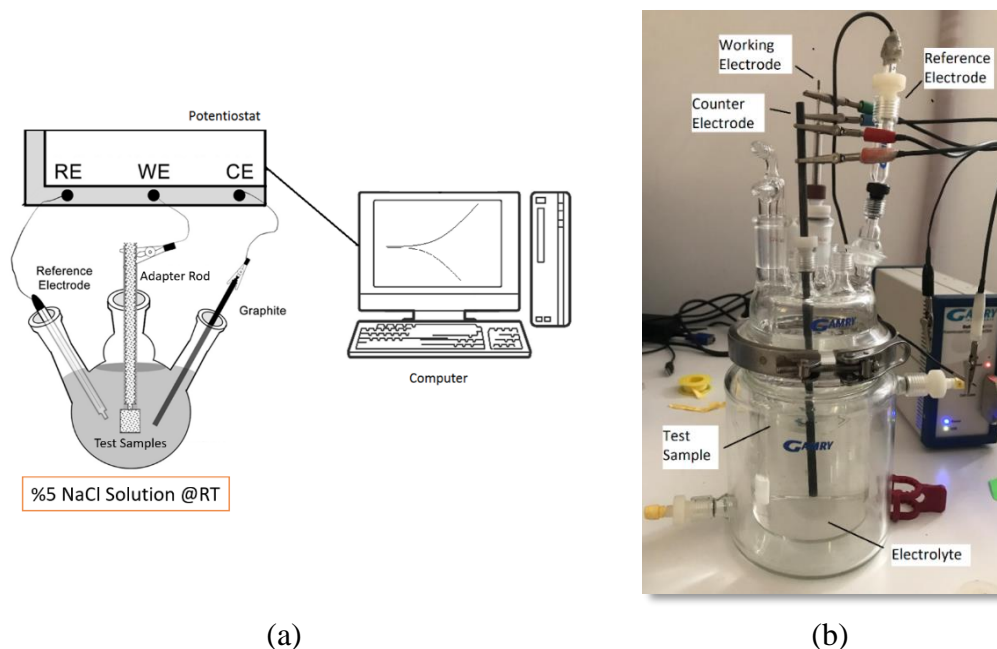


Figure 3.7. Potentiodynamic polarization test setup: (a) A schematic test setup and connections (b) Gamry multiport kit with jacketed for electrochemical corrosion cell.

The test setup and test parameters as shown in Table 3.3. for the aluminum alloy and CFRP samples were established. After aluminum alloy was immersed in the solution, it was left in the electrolyte for one day to reach stable open circuit potential. Then, the test parameters were entered into the system, and potentiodynamic test results were observed. Then, the test setup was installed for the CFRP sample. Likewise, after immersing the sample in the electrolyte solution, it was held in the electrolyte for a day until it reached stable open circuit potential. By entering the experiment parameters, a potential dynamic test scan was initiated, and data were received.

Table 3.3. *Potentiodynamic test setup for samples.*

Potentiodynamic Test Setup for AA2024-T3	
Port Name	Material
Working Electrode	AA2024-T3
Counter Electrode	Graphite
Reference Electrode	Saturated Calomel Electrode (SCE)
Electrolyte	% 5 NaCl @RT
Parameters	Values
Initial E (V)	-1.7
Final E (V)	-0.3
Scan Rate (mV/s)	5
Sample Period (s)	1
Sample Area (cm ²)	1
Potentiodynamic Test Parameters for CFRP	
Port Name	Material
Working Electrode	CFRP
Counter Electrode	Graphite
Reference Electrode	Saturated Calomel Electrode (SCE)
Electrolyte	%5 NaCl @RT
Parameters	Values
Initial E (V)	-0.1
Final E (V)	0.5
Scan Rate (mV/s)	5
Sample Period (s)	1
Sample Area (cm ²)	1

3.2. Laboratory Immersion Corrosion Testing

Immersion corrosion laboratory tests are used to obtain information about the corrosion resistance of the materials quickly. The factors such as environmental temperature and the humidity that the materials can be exposed during the service can be simulated, and the corrosion resistance of the materials in service conditions can be predicted [48].

3.2.1. Materials

Aluminum alloy AA2024-T3 (SAE AMS QQ-A-250/5) clad sheet of 0.5 mm thickness and 45x100 mm dimensions and CFRP (Carbon-fiber-reinforced plastic) epoxy prepreg 120°C cure material having 0.5 mm thickness and 45x100 mm dimensions were joined as shown in Figure 3.8. by A resin based coated (RBC) titanium bolt which was galvanically compatible with both materials was used in joining.

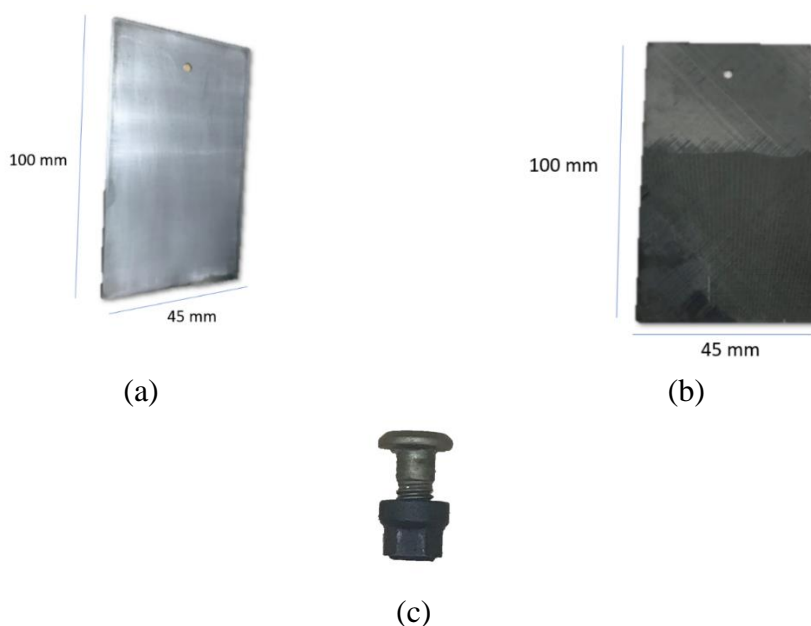


Figure 3.8. Immersion corrosion test elements in %5 NaCl solution @RT (a) AA2024-T3; (b) CFRP; (c) RBC coating Titanium bolt.

3.2.2. Sample Preparation

The glass layer adhered as a protective layer on the carbon fiber material was removed with P4000 sandpaper to ensure electrical conductivity when it is in contact with aluminum. The conductivity was checked with a digital multimeter. The surface of aluminum material was ground with P1200 and P4000 sandpaper to remove the clad structure. Then it was joined together with the help of a titanium bolt as seen in Figure 3.9. They were controlled with the help of a digital multimeter to ensure that materials were electrically connected continuously ($<30.0\text{k}\Omega$).

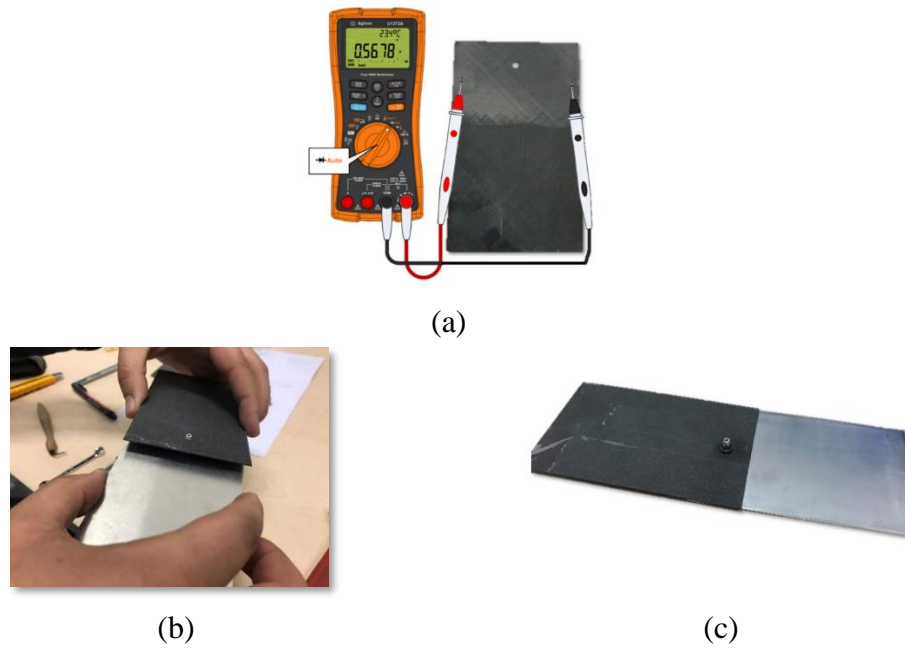


Figure 3.9. Preparation steps of the test sample (a) Continuity control for CFRP after the glass layer was removed from the surface (b) Combining AA2024-T3 and CFRP material with RBC coating Titanium bolt (c) Final test sample.

3.2.3. Electrolyte

A 5% NaCl solution, also used in the potentiodynamic polarization test, was used to represent the maximum environmental impact the materials would be exposed to in the aircraft. In order to represent the hazardous area, as shown in Figure 3.6, the immersion test was carried out with a solution 5 mm above the test materials.

3.2.4. Test Setup

To observe the galvanic corrosion effect, firstly, the prepared material system was cleaned with water and alcohol, carefully dried so that no moisture remained, then immersed in NaCl solution. Three sets of test devices, having 3 pieces each were grouped, totally 9 samples, placed in a plastic container that was not affected by corrosion for 3, 15, and 45 days, respectively, and the 5 mm solution level was

continuously controlled with the help of a ruler and maintained at that level as shown in Figure 3.10.

The stabilization and maintenance of the electrolytic conductivity of solution at a constant value during the experimental study and modeling was achieved by regularly renewing and controlling depending on the immersion days. After the immersion test, the joints were again purged with water and ethanol and finally dried. Then the materials were separated from each other, and the pit corrosion caused by galvanic coupling on aluminum alloy was examined by electron microscope (Zeiss Gemini Field Emission Gun). Furthermore, surface topology was investigated to examine the surface by a digital microscope (ZEISS Smartzoom 5).

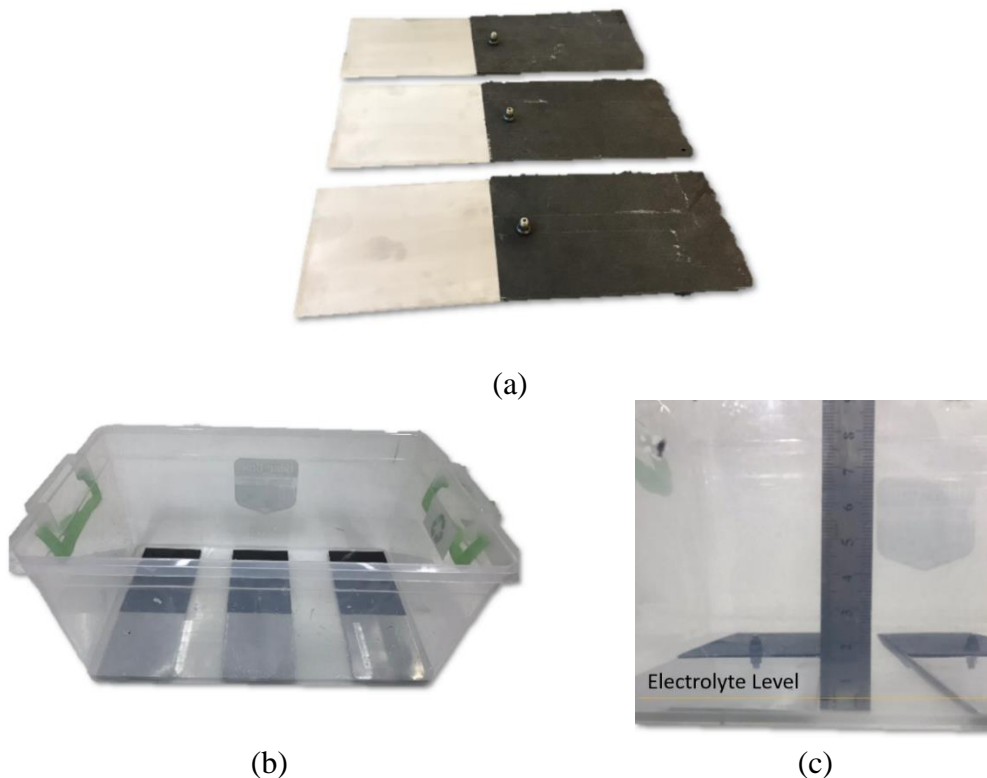


Figure 3.10. Test setup for corrosion immersion test and electrolyte control mechanism (a) Test samples (b) Test setup (c) Electrolyte level control.

3.3. Numerical Modelling

COMSOL Multiphysics 5.2 software was used to model galvanic corrosion between aluminum alloy AA2024-T3 and CFRP material under 5 mm NaCl electrolyte thickness for 3, 15 and 45 days. With the help of potentiodynamic measurement results as input to the system, the potential distribution, local current density on aluminum and carbon fiber material, and electrolyte thickness change were taken as output. The bolt used to combine aluminum alloy and carbon fiber material was not included in the modeling because it is galvanically compatible with both materials and was far from the surface corrosion observed.

3.3.1. Setting Model Environment

For this modeling, the deformable geometry corrosion module of the Comsol software was chosen. As the interface, a secondary corrosion module was used, which gives current, potential distribution and geometrical changes in the corrosion cell, neglecting the compositional changes in the electrolyte solution. This module uses secondary current distribution and deformable geometry as shown in Figure 3.11.

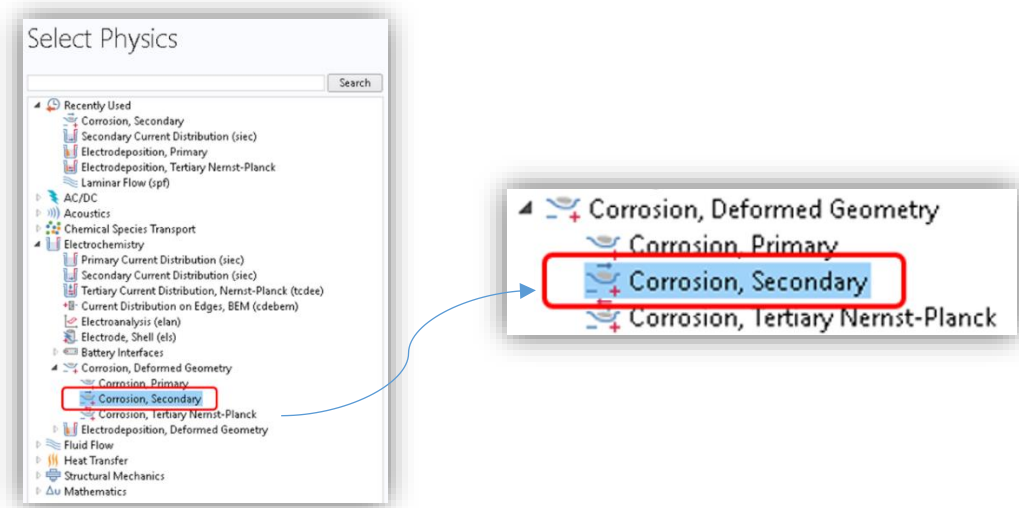


Figure 3.11. Selecting physics for modelling (The picture was taken as screenshot from Comsol software).

3.3.2. Creating Geometric Object

The model geometry is shown in Figure 3.12 . A single domain electrolyte was used. The left part of the bottom boundary is the surface of the CFRP material; the right part is the corroding aluminum AA2024-T3 alloy. Since the AA2024-T3 aluminum alloy corrodes in the model, the right boundary is displaced downwards in the geometry. A small height step of 0.025 mm in the negative y-direction was added at the starting point of the geometry to maintain the topology of the geometry during the simulation. The vertical limit of the step was assumed that belongs to the CFRP surface.

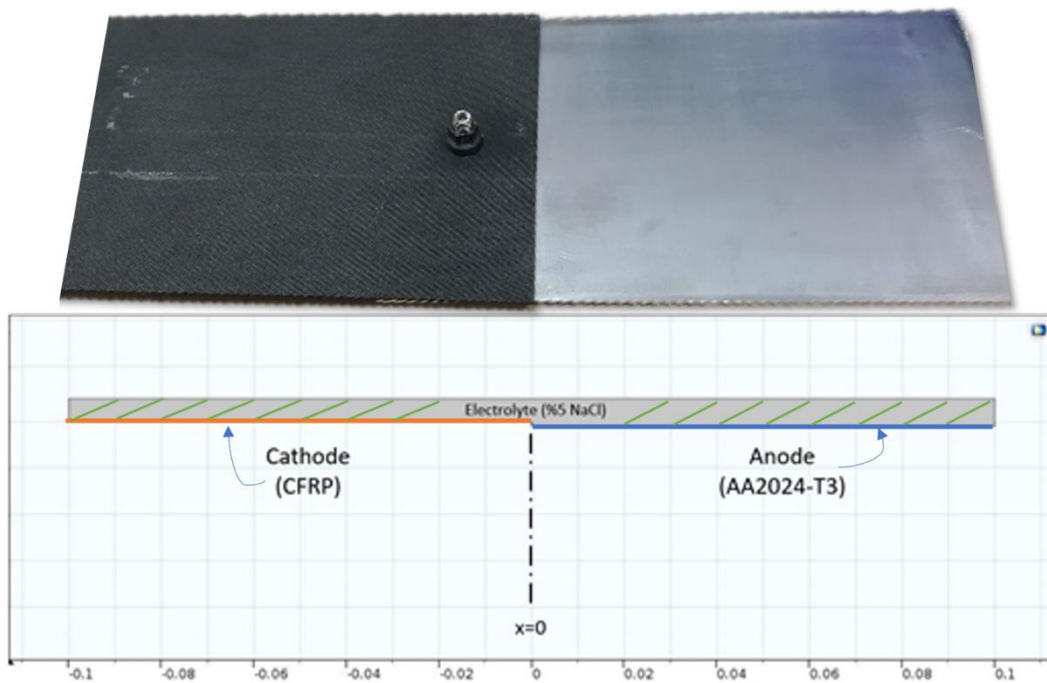
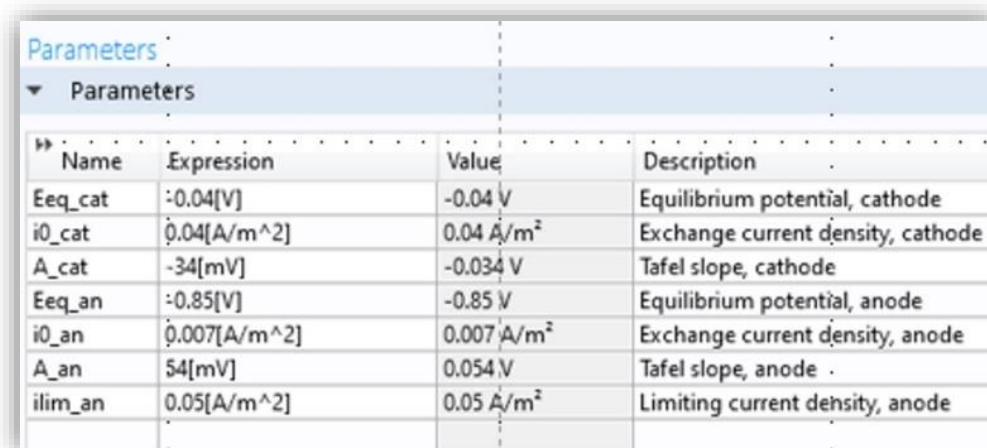


Figure 3.12. Model geometry.

3.3.3. Specifying Properties of Materials

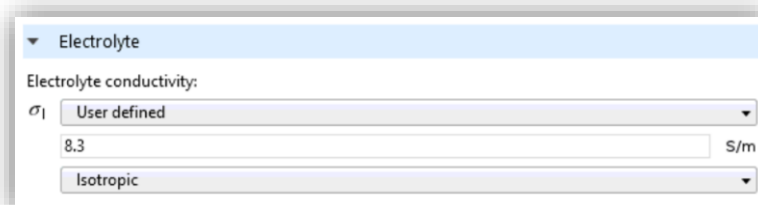
Electrochemical properties (equilibrium potential, exchange current density, Tafel slope constant and limiting current density) of aluminum and carbon fiber material found as a result of potentiodynamic measurements were entered into the model as shown in Figure 3.13. Since aluminum is highly anodic compared to CFRP in the galvanic series, CFRP acts as the cathode while aluminum as the anode.



Name	Expression	Value	Description
Eeq_cat	-0.04[V]	-0.04 V	Equilibrium potential, cathode
i0_cat	0.04[A/m^2]	0.04 A/m ²	Exchange current density, cathode
A_cat	-34[mV]	-0.034 V	Tafel slope, cathode
Eeq_an	-0.85[V]	-0.85 V	Equilibrium potential, anode
i0_an	0.007[A/m^2]	0.007 A/m ²	Exchange current density, anode
A_an	54[mV]	0.054 V	Tafel slope, anode
ilim_an	0.05[A/m^2]	0.05 A/m ²	Limiting current density, anode

Figure 3.13. Material parameters (The picture was taken as screenshot from Comsol software).

Since the 5% NaCl solution is homogeneously mixed, the secondary flow distribution equation can be used because it exhibits the same properties, or the properties are not dependent on the direction (Isotropic conductivity) throughout, while solving for the electrolyte potential, Φ_1 (V), in the domain. The conductivity of the electrolyte measured as 8.3 S/m (see) was entered into the model as can be seen in Figure 3.14.



Electrolyte

Electrolyte conductivity:

σ_1 User defined

8.3 S/m

Isotropic

Figure 3.14. Electrolyte conductivity (The picture was taken as screenshot from Comsol software).

3.3.4. Defining Physics Boundary Conditions

Electrochemical responses are chemical responses that include discharge and take-up of electrons from/to an external circuit. One electrode acts overwhelmingly as an anode (electron and cation creating). It is the component of the galvanic couple that experiences material disintegration. In contrast, the other acts overwhelmingly as a cathode and is the location where a cathodic (electron and anion expending) response takes place. The electrons delivered by the anodic response are precisely utilized up by anions at the cathode by the cathodic response.

Galvanic corrosion is an electrochemical action that happens when at most two different metals are in electrical contact with one another. The sum and rate of disintegration of the anode material are specifically related to the electrochemical potential dispersion at the anode-electrolyte interface.

Electrode Reaction on Cathode

Since the equilibrium potential of AA2024-T3 is -0.85V and CFRP is -0.04V from the potentiodynamic polarization resistance measurement, CFRP will act as a cathode in the galvanic couple formed by these two materials. In the model, the surface was defined as shown in Figure 3.15 so that there is a cathodic reaction on the CFRP material surface.

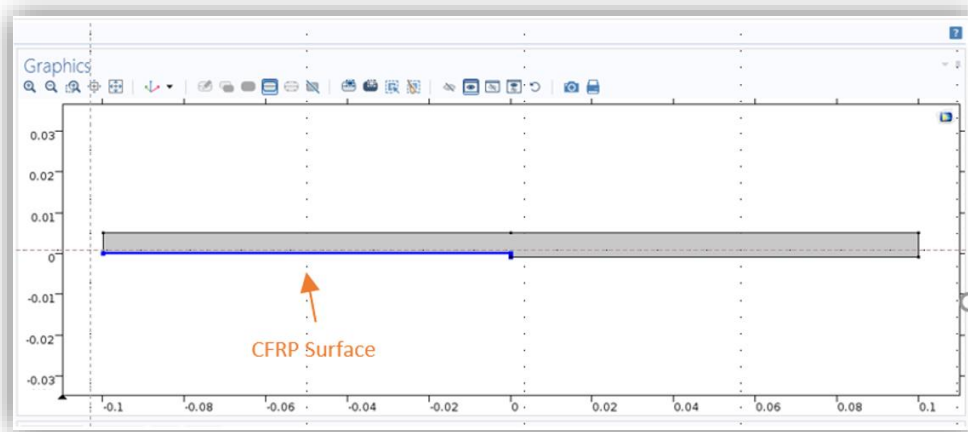


Figure 3.15. Cathode (CFRP) reaction surface.

The cathodic Tafel expression shown below was used to describe the reaction kinetics herein [49] and also shown in Figure 3.16.

$$i_{cat} = -i_{0,cat} \cdot 10^{\frac{\eta}{A_{cat}}} \quad (25)$$

Where $i_{0,cat} = 4 \times 10^{-2} \text{ A/m}^2$ is the exchange current density of cathode (CFRP), and $A_{cat} = -34 \text{ mV}$ from the Tafel slope of CFRP cathodic reaction.

The overpotential of electrode reaction for cathode is expressed as η (unit: V)

$$\eta = \Phi_s - \Phi_1 - E_{eq,cat} \quad (26)$$

Where Φ_s is the cathodic material (CFRP) potential and Φ_1 is the electrolyte potential in the electrode. $E_{eq,cat}$ is the equilibrium potential (-0.04V) for the cathode material (CFRP)

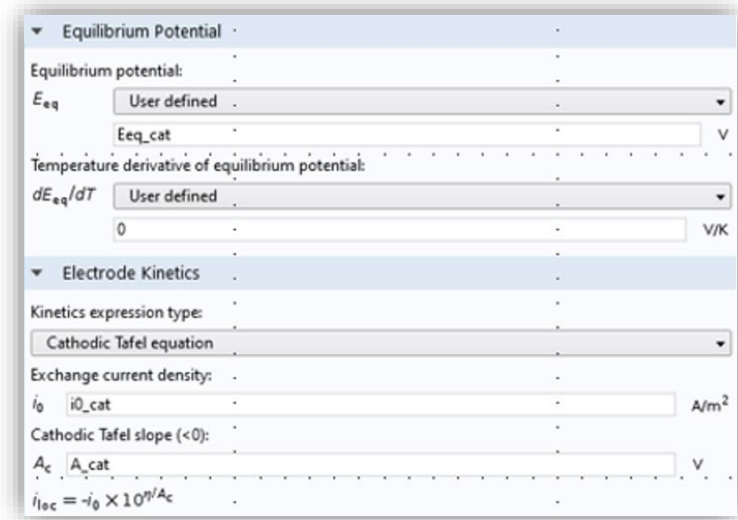


Figure 3.16. Cathode (CFRP) reaction parameters (The picture was taken as screenshot from Comsol software).

Electrode Reaction on Anode

In an AA2024-T3 and CFRP galvanic pair, aluminum will act as anode, and anodic reactions will take place on aluminum material. In the model, the anode surface was defined as seen in Figure 3.17.

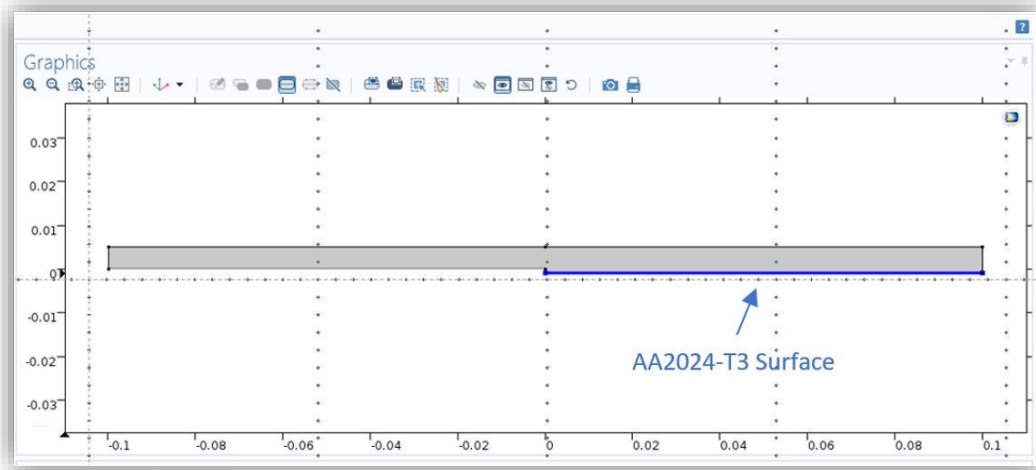


Figure 3.17. Anode (AA2024-T3) reaction surface.

Oxidizing of aluminum takes place according to:



Since the main element forming the AA2024-T3 alloy is aluminum, the oxidation reaction of other alloying elements in the alloy were neglected.

Diffusion limited anodic Tafel equation was used for anode electrode reaction as described below [49]:

$$i_{tafel} = i_{0,an} \cdot 10^{\frac{\eta}{A_{an}}} \quad (28)$$

Under assumption of Nernstian diffusion layer and first order dependence of concentration, reaction can be stated as:

$$i_{an} = \frac{i_{lim}}{1 + \frac{i_{lim}}{i_{tafel}}} \quad (29)$$

Where $i_{0,an} = 7 \times 10^{-3} \text{ A/m}^2$, $A_{an} = 54 \text{ mV}$ (Tafel slope of anodic reaction of AA2024-T3), and $i_{lim} = 5 \times 10^{-2} \text{ A/m}^2$ (Limiting current density)

As the aluminum dissolves in by the anodic reaction, the electrode boundaries move at a velocity v (m/s), consequently

$$v = \frac{i_{an} M}{2F \rho} \quad (30)$$

Where F is the Faraday constant, M is the mean molar mass g/mol and ρ is the density of aluminum alloy.

Anode reaction parameters were entered into the model as shown in Figure 3.18.

Electrode Reaction

Equation

Show equation assuming:

Study 1, Current Distribution Initialization

$\eta = \phi_{s,ext} - \phi_l - E_{eq}$

Model Inputs

Temperature:

T User defined

293.15[K] K

Materials

Equilibrium Potential

Equilibrium potential:

E_{eq} User defined

Eeq_an V

Temperature derivative of equilibrium potential:

dE_{eq}/dT User defined

0 V/K

Electrode Kinetics

Kinetics expression type:

Anodic Tafel equation

Exchange current density:

i_0 i0_an A/m²

Anodic Tafel slope (>0):

A_a Aa_an V

$i_{exp} = i_0 \times 10^{\eta/A_a}$

☒ Limiting current density

i_{lim} ilim_an A/m²

$i_{loc} = \frac{i_{lim} i_{exp}}{i_{lim} + |i_{exp}|}$

Stoichiometric Coefficients

Number of participating electrons:

n_m 3 1

Stoichiometric coefficients for dissolving-depositing species:

Species	Stoichiometric coefficient (1)
Al	1

Figure 3.18. Anode (AA2024-T3) reaction parameters (The picture taken as screenshot from Comsol software).

Non-Deforming Boundary

Since only corrosion on the aluminum anode surface will be observed, all other surfaces except the anode surface have been identified as non-deformable boundaries as shown in Figure 3.19.

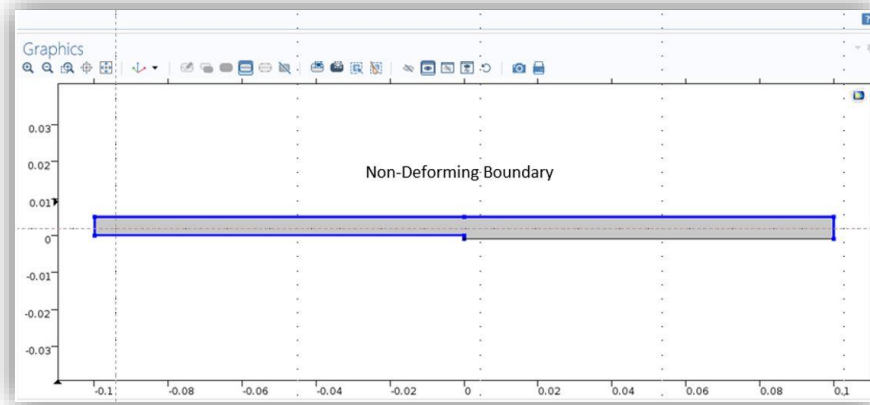


Figure 3.19. Non-Deforming boundaries on model (The picture was taken as screenshot from Comsol software).

These non-deforming boundary surfaces will have zero normal displacement as boundary conditions in modeling. Non-deforming boundary parameters were entered into the model as seen in Figure 3.20.

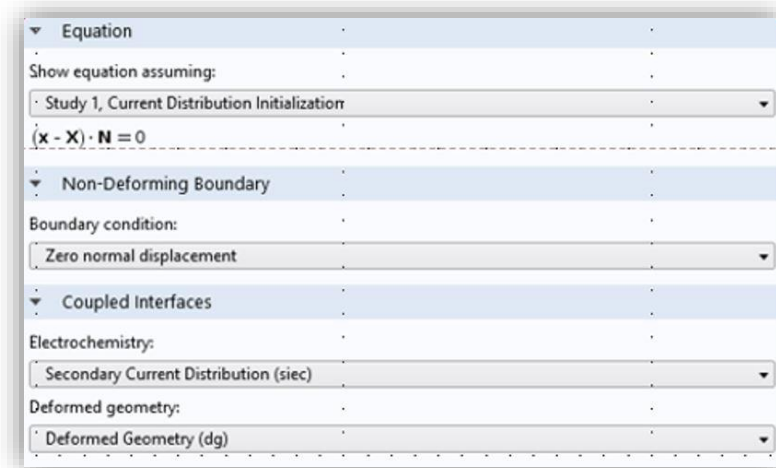


Figure 3.20. Non-Deforming boundary parameters (The picture was taken as screenshot from Comsol software).

Deforming Electrode Surface

The deformable surface is defined on the aluminum surface where the deterioration will occur, as seen in the Figure 3.21.

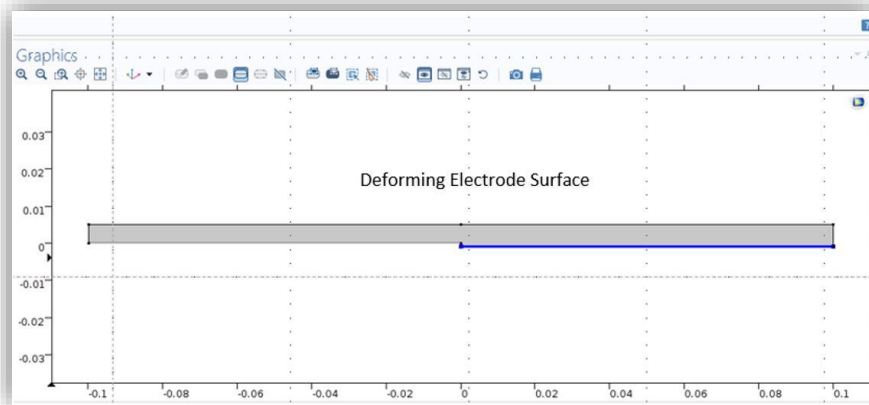


Figure 3.21. Deforming electrode surface on model (The picture was taken as screenshot from Comsol software).

The parameters used to define the deformed surfaces are shown in Figure 3.22. The software's moving boundary smoothing feature was activated to get better results while moving the boundaries.

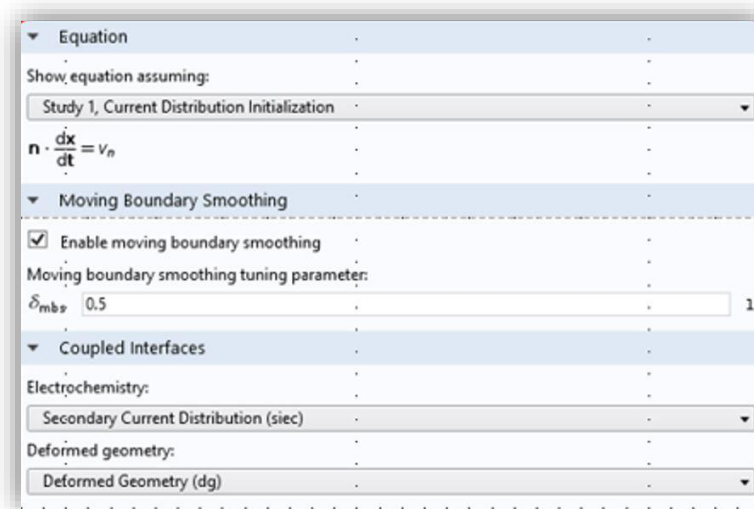


Figure 3.22. Deforming electrode surface parameters (The picture was taken as screenshot from Comsol software).

3.3.5. Creating Mesh

Meshing the model geometry is one of the critical steps of the simulation processes because all the operations in modeling are done over these small meshes as seen in Figure 3.23. The tetrahedral mesh was used as the mesh type, and the finer mesh was used as the size (Complete mesh consists of 175 elements. Minimum quality: 0.6957, average quality 0.8978). Since the region to examine is the junction region, more meshes were used here to get better results [50].

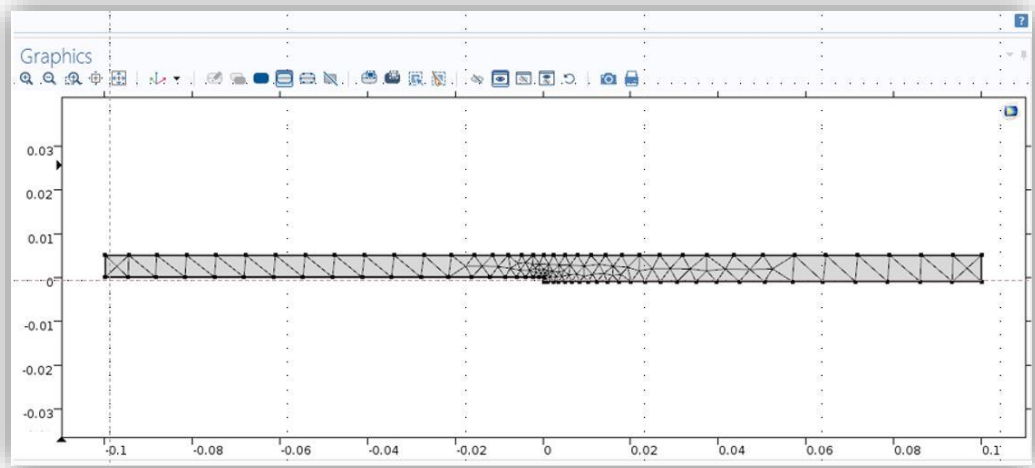
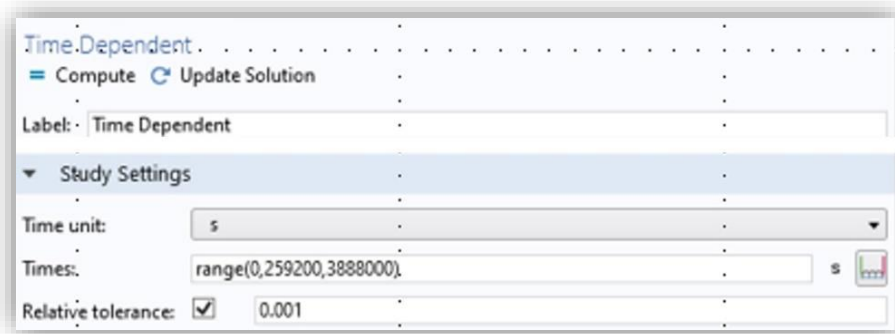
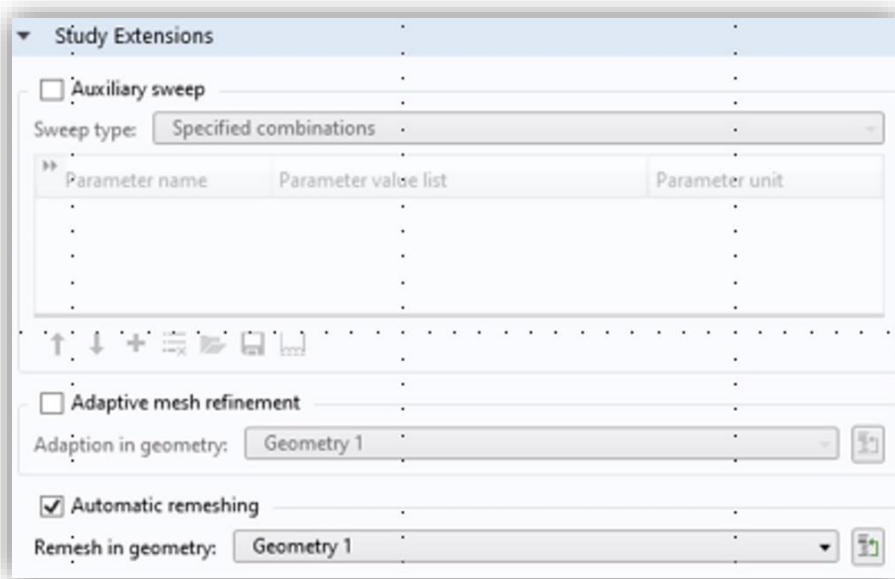


Figure 3.23. Mesh on model (The picture was taken as screenshot from Comsol software).

The time-dependent simulations were performed for 3, 15 and 45 days to replicate immersion test times. The automatic remeshing option was chosen as the dissolution system of the meshes, and the deviations from the mesh in the results were minimized as shown in Figure 3.24.



(a)



(b)

Figure 3.24. Automatic remeshing option and time dependent study (a)Time dependent parameters;
(b) Automatic remeshing option (The picture was taken as screenshot from Comsol software).

CHAPTER 4

RESULTS AND DISCUSSION

4.1. Results of Potentiodynamic Polarization Resistance Measurements

The potentiodynamic polarization graphs of aluminum AA2024-T3 and CFRP materials are shown in Figure 4.1 and Figure 4.2, respectively.

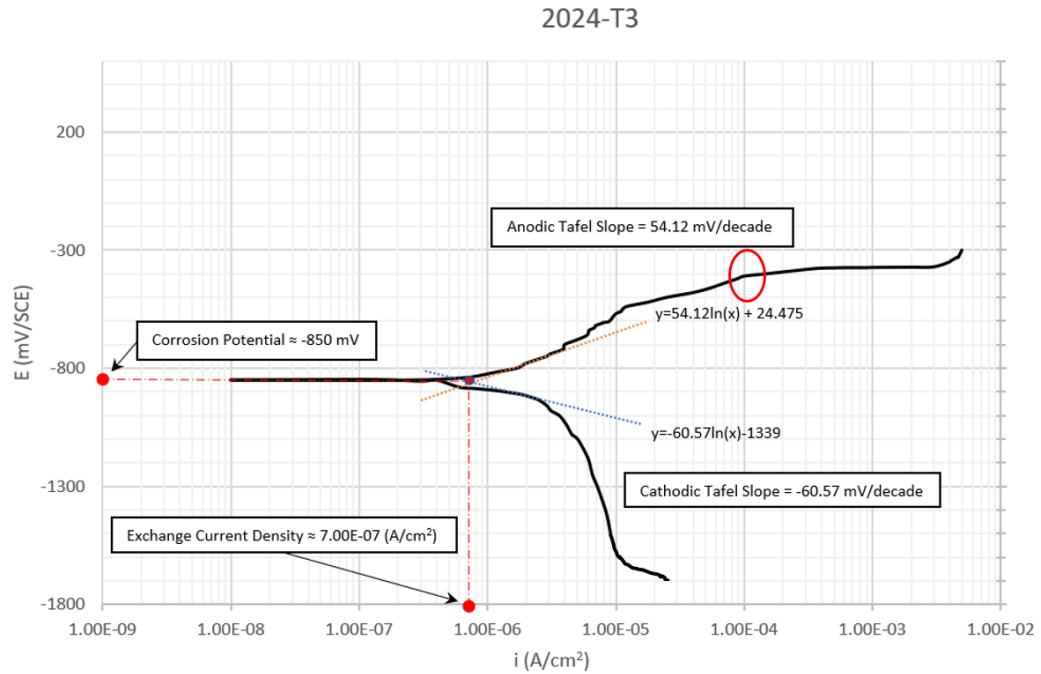


Figure 4.1. Potentiodynamic polarization measurement for AA2024-T3.

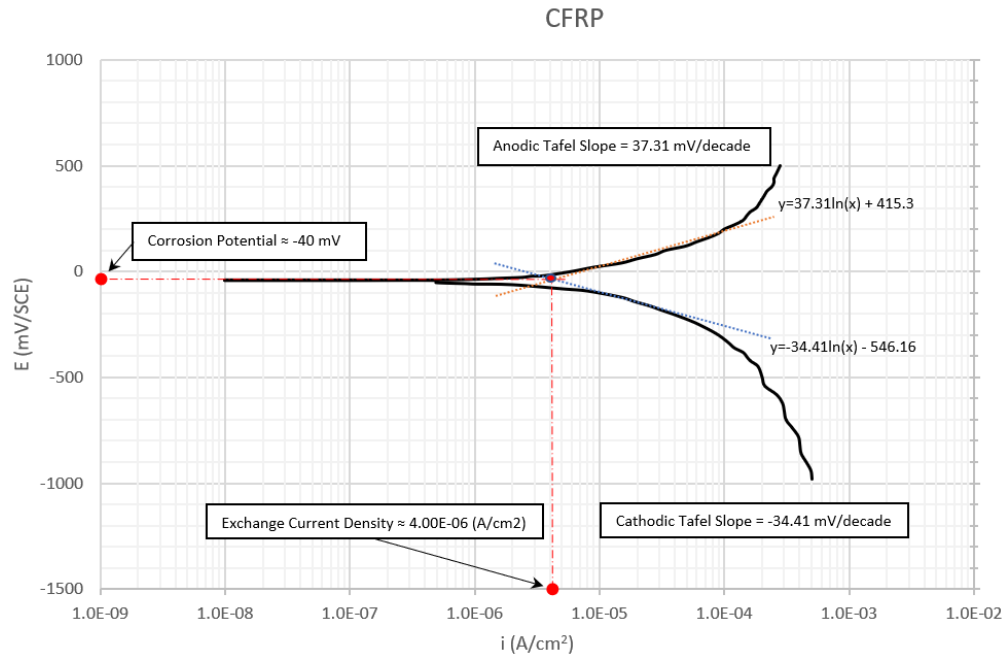


Figure 4.2. Potentiodynamic polarization measurement for CFRP.

As can be seen in Figure 4.1, the scanning process for 2024-T3 was started at -1700 mV and continued up to -300 mV. Open circuit potential, in other words, equilibrium corrosion potential ($E_{\text{corr,AA2024-T3}}$), was observed at about -850 mV (SCE) and exchange current density ($i_{\text{corr,AA2024-T3}}$), was observed at about $7.00\text{E-}07 \text{ A/cm}^2$. The scanning interval for CFRP material was started at -1000 mV and continued up to 500 mV, as seen in Figure 4.2. Open circuit potential ($E_{\text{corr,CFRP}}$) was approximately at -40 mV (SCE) and exchange current density ($i_{\text{corr,AA2024-T3}}$), was approximately at $4.00\text{E-}06 \text{ A/cm}^2$. At E_{corr} point, the sum of the anodic and cathodic reaction rates on the material surface is zero. For this reason, the total current value is approximately zero.

As the equilibrium begins to move away from the potential of corrosion, this area is called the Tafel region, anodic and cathodic slopes are constant in this region. In the Tafel analysis approach, the intersection point will theoretically give the corrosion current density as a result of extrapolating linear changes in the anodic and cathodic regions. This linear field may not be provided precisely in many real corrosion systems.

Gamry eChem software gives β_a (Tafel slope, anode) and β_c (Tafel slope, cathode) values to fit experimental data to Butler-Volmer equation as shown in Table 4.1. Since the Chi-square parameter is about 187×10^{-3} . It can be understood that the data fit well with this equation.

Table 4.1. The overall Tafel slopes obtained from potentiodynamic tests for AA2024-T3 and CFRP.

Materials	β_{Anode} (mV/decade)	β_{Cathod} (mV/decade)
AA2024-T3	54.12	-60.57
CFRP	37.31	-34.41

4.1.1. Critical Pit Current Density

As the potential applied for aluminum alloy after the Tafel zone increases in the anodic screening zone, the pitting corrosion on the material surface starts locally. Still, the oxide layer formed by the aluminum on its surface is not entirely broken [51].

When the applied potential increased sufficiently, the critical current density value of $1.0\text{E-}4 \text{ A/cm}^2$ is enclosed in the red circle in Figure 4.1. At the same time, as seen in the graph drawn near the critical region in Figure 4.3, the current of corrosion started to increase very rapidly.

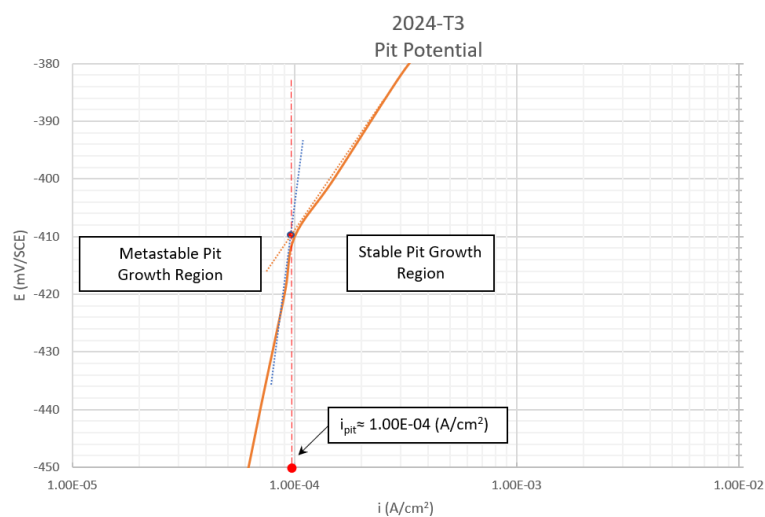


Figure 4.3. AA2024-T3 Potentiodynamic polarization critical current.

It can be concluded like very similar example of shown as Figure 4.4 from H. Böhni [52] that the pitting corrosion formed after this value occurs stably. For this reason, we can assume that the oxide layer on aluminum breaks at current density values above this value, and pitting corrosion continuously occurs. One can consider this critical current density value ($i_{pit} \approx 1.0E-4 \text{ A/cm}^2$) as the minimum value required for the formation of pitting corrosion.

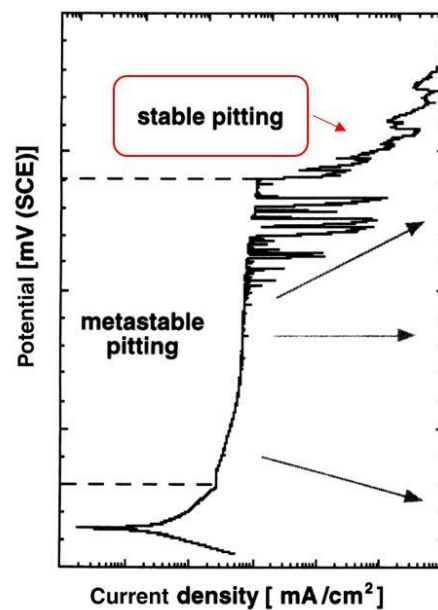


Figure 4.4. Example of stable and metastable pitting potential curve of a passive metal (The graph is reproduced from the *source* [52])

4.1.2. Limiting Current Density

In a reaction, two main kinetic factors control the reaction rate. First, charge transfer is also called activation control. As long as the driving force is available, the reaction rate is controlled according to the size of the power (for example, hydrogen development reaction or the water indication reaction). The reaction speed increases as long as the driving force increases, but this does not go on forever. Second, due to mass transfer from the mechanisms controlling the reaction rate, the reaction rate is controlled depending on the diffusion rate from the electrolyte to the electrode surface.

At a certain point, the current density value has reached the maximum. This current density value depends on the diffusion functions of the concentrations of the species in the electrolyte. Even if the applied potential force is increased, the reaction rate will not increase [53].

When the cathodic scanning curve formed on aluminum alloy is examined in Figure 4.1, it reflects the oxygen reduction reaction between -0.8 and -1.6 V values depending on the pH level in the electrolyte and the amount of dissolved oxygen. The resulting reaction rate will occur at a specific upper limit, depending on how fast the oxygen molecules diffuse (mass transport control). This is known as the limiting current density, which is the factor that controls the reaction rate.

In diffusion-controlled cathodic reactions, the limiting current density value is an important parameter since it determines the reaction rate. The plateau part formed in the curve obtained from the first derivative of the current density potential curve, which is one of the methods suggested by Ponce de Leon [54] to find the limiting current density value, may be composed of a combination of hydrogen formation and oxygen reduction on the cathodic surface. This situation corresponds to the inflection point in the current density potential curve. This value corresponds to approximately $i_{lim,an} \approx 5.0E-6 \text{ A/cm}^2$ for aluminum.

When the potential value applied reaches a sufficiently negative value for the cathodic reaction (-1.6 V in Figure 4.1), the thermodynamic thrust force causes additional cathodic reactions. When this potential is further increased, this reaction, which occurs in the range of -1.6 to -1.7 volts in Figure 4.1, becomes dominant. Such extra reactions usually involve the reduction of other species in the electrolyte. Probably the water reduction reaction became dominant in this region.

4.1.3. Mixed Potential Theory

Theoretically, a mixed potential approach can be used to find the galvanic corrosion current and potential values on the AA2024-T3 and CFRP pair. In this theory, when two or more electrochemical reactions occur simultaneously, the potential of the resulting corrosion can be defined as the potential of the entire system. When the total current density of the realized anodic and cathodic reactions is zero, the current and potential values at this point can be evaluated as the current and potential values of the system.

Wagner and Traud [29] state that the potential and current density value of the galvanic corrosion system can use the intersection points of anodic and cathodic potential current polarization curves in the system as shown in Figure 4.5. When this approach is applied, the mixed corrosion potential of the AA2024-T3 and CFRP material pair can be defined as $E_{\text{Corr,couple}} \approx -0.4 \text{ V (SCE)}$ and the mixed current density value $i_{\text{Corr,couple}} \approx 1.5\text{E-}4 \text{ A/cm}^2$.

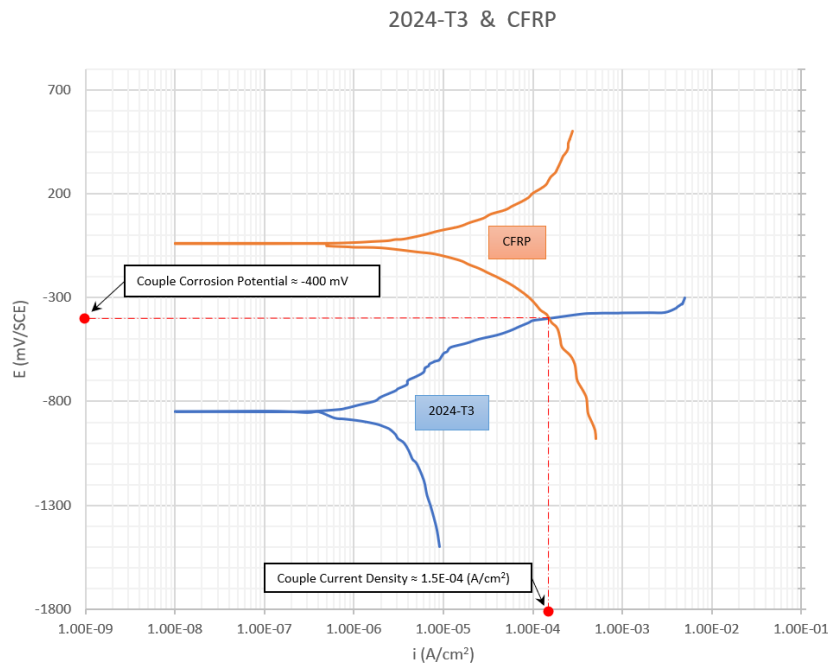


Figure 4.5. Potentiodynamic polarization curves for mixed AA2024-T3 and CFRP.

4.2. Laboratory Immersion Corrosion Test Results

Nine test samples, three sets for each immersion duration, were kept in %5 wt NaCl solution for 3, 15 and 45 days. The samples were then examined from the region where two distinct materials were connected to each other as shown in red in Figure 4.6. For the pitting corrosion caused by the galvanic corrosion effect on the aluminum surface, the critical distance from the junction and the maximum depth formed were determined.



Figure 4.6. The region where the galvanic corrosion effect was examined on the aluminum AA2024-T3.

4.2.1. Critical Pit Distance

The critical pitting corrosion distance was determined based on the pitting corrosion seen at the maximum distance from the aluminum alloy and CFRP junction. The junction between aluminum alloy and CFRP was scanned through the test sample by a digital microscope (ZEISS Smartzoom 5). The results found for all test samples can be seen in Table 4.2 below.

Table 4.2. Critical pit distance on AA2024-T3 from the joint in microns (The maximum values were shown in Bold).

Critical Pit Distance (μm)			
Test Samples	3 Days	15 Days	45 Days
Test Sample 1	2460	-	-
Test Sample 2	2880	-	-
Test Sample 3	2100	-	-
Test Sample 4	-	4830	-
Test Sample 5	-	4390	-
Test Sample 6	-	3740	-
Test Sample 7	-	-	5000
Test Sample 8	-	-	4790
Test Sample 9	-	-	4530
Average	2480	4320	4773

Maximum critical pit distances on AA2024-T3 from the joint line with CFRP after 3, 15 and 45 days are visible from the pictures as shown in Figure 4.7, Figure 4.8, and Figure 4.9, respectively.

As expected, the density of pitting corrosion caused by galvanic corrosion, which occurred after three days, was low, and the critical distance is approximately 2880 microns. The dark and united dots seen in Figure 4.7 were caused by galvanic corrosion. Moving from the junction point to the inner side of AA2024-T3, separate corrosion points are also seen.

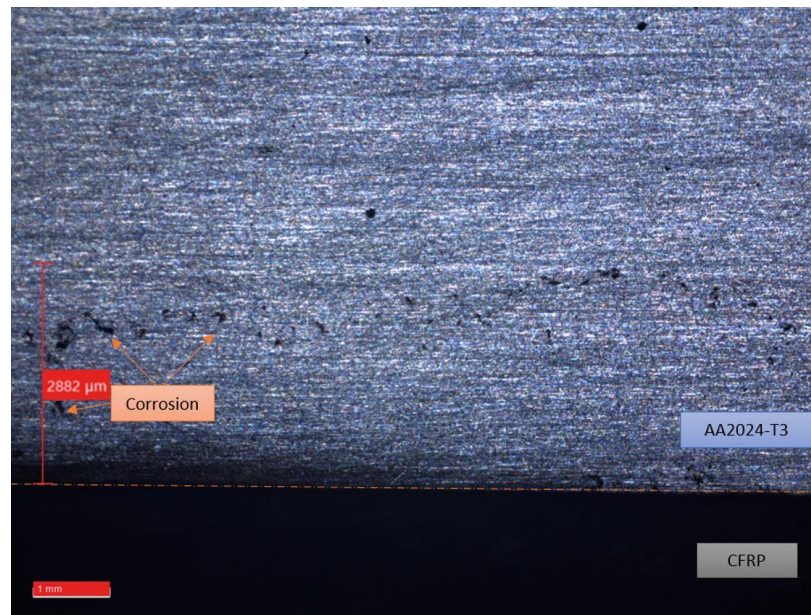


Figure 4.7. Maximum critical pit distance sample 2 after 3 days immersion test.

It can be said that the pit corrosion caused by galvanic corrosion at the end of 15 days, is more severe than the 3-day results as shown in Figure 4.8. Notably, the corrosion intensity at the junction is higher, and also corrosion depth is further away (4828 microns) from the junction.

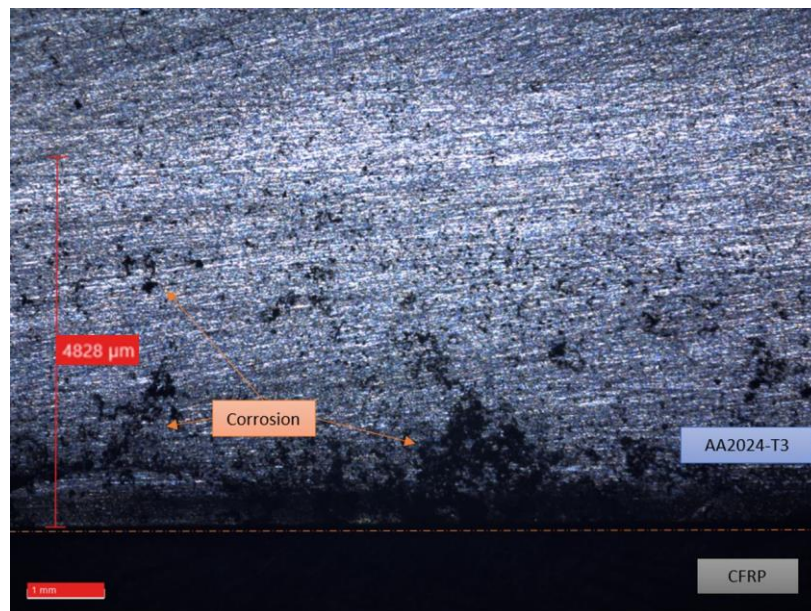


Figure 4.8. Maximum critical pit distance sample 4 after 15 days immersion test.

When the 45-day dipping test samples are analyzed, it is seen that the pitting corrosion density was at the highest level as shown in Figure 4.9. Although the pitting density increased compared to the 15-day test, the critical pit corrosion distance (5000 micron) was similar.

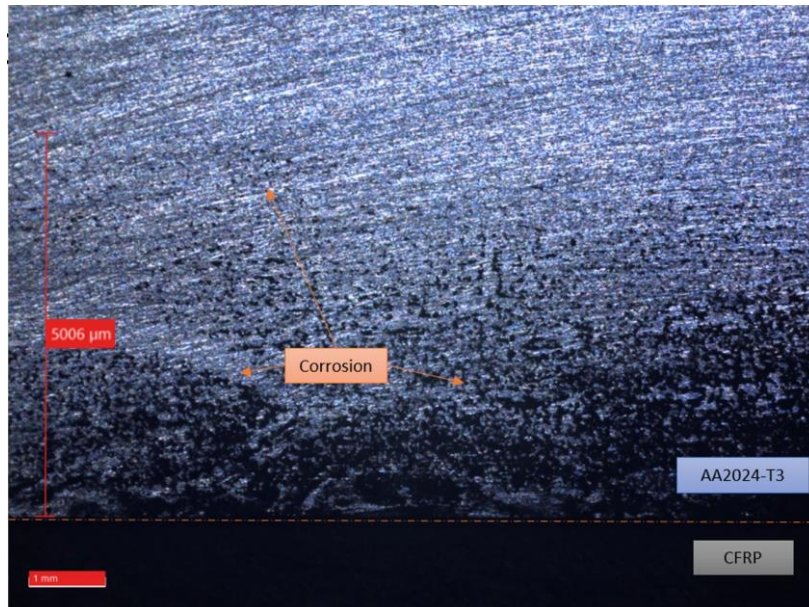


Figure 4.9. Maximum critical pit distance sample 7 after 45 days immersion test.

Characterization of Pits

After the immersion tests, the surfaces of the samples near the junction were examined by the electron microscope (ZEISS GeminiSEM). The SEM photograph of sample 2 from 3 days immersion test is given in Figure 4.10 . As can be seen in this photo, the pits formed on the aluminum alloy surface are visible. The corrosion products formed as a result of galvanic corrosion are seen as white deposit and they do not go away after cleaning with ethanol after the test.

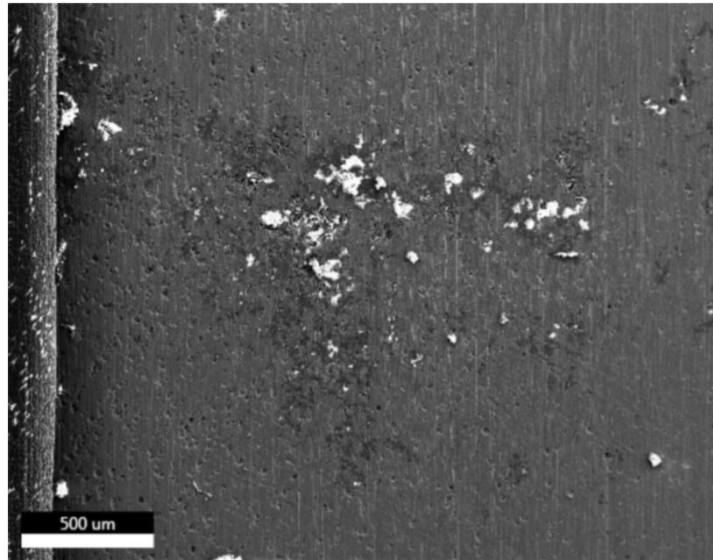


Figure 4.10. A typical SEM (Scanning electron microscope) image of joint area of test sample 2 subjected to immersion test for 3 days.

Elemental mapping (Figure 4.11) and quantitative (Figure 4.12) analyzes were performed on the image taken from the junction point to characterize the resulting corrosion products. As expected, there is an increase in oxygen concentration at the places where corrosion has occurred. The corrosion product was most probably $\text{Al}(\text{OH})_3$ due to the aqueous environment. Carbon comes from carbon fiber material and copper is one of the alloying elements of the AA2024-T3 alloy.

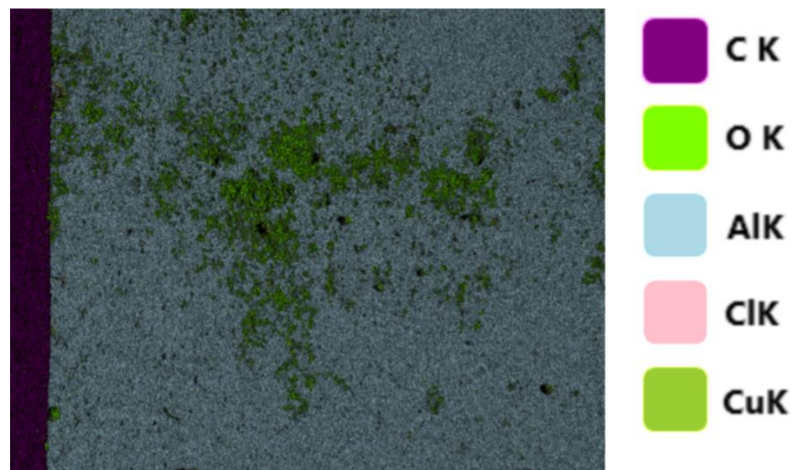


Figure 4.11. Elemental mapping analysis of joint area.

It should be noted that the quantitative analysis result given in Figure 4.12 is not reliable for oxygen element, as it is a light element.

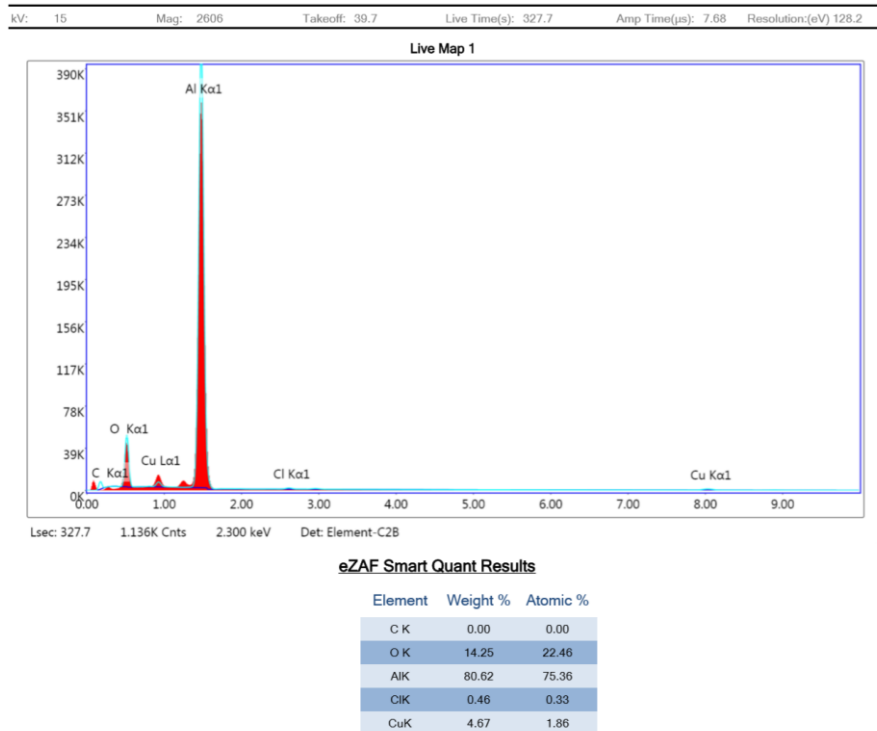


Figure 4.12. Quantitative elemental analysis of joint area.

4.2.2. Maximum Pit Depth

To measure the maximum pitting depth caused by galvanic corrosion between aluminum and carbon fiber material, ASTM G-46 [55] (Standard Guide for Examination and Evaluation of Pitting Corrosion) section 4.1.5 Metallographic Examination method was used. Three places from the aluminum surface at the maximum distance seen in the critical pitting distance measurement (Section 4.2.1) were first cut, as shown in Figure 4.13a. Then, the samples containing the pits that were formed during the tests were positioned to measure the depth of corrosion by looking at the edge of the section with bakelite (Figure 4.13b) and conductive bakelite

(Figure 4.13c). The prepared samples with P4000 paper were then examined under the electron microscope to determine the depth of the pitting corrosion.

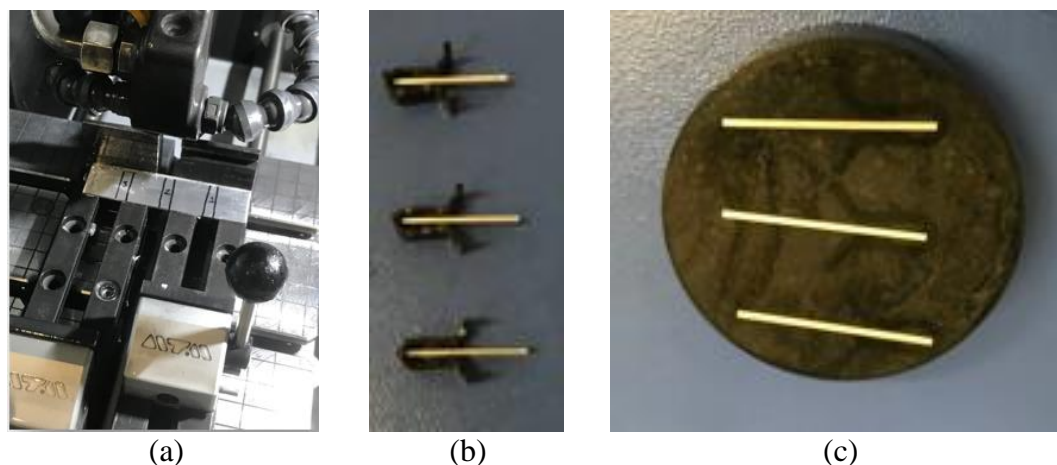


Figure 4.13. Sample preparation steps to measure maximum pit depth (a) Cutting step; (b) Cross-section sample; (c) Conductive bakelite step.

The same operations were done for samples that were immersed for 3, 15 and 45 days, and the pits having the highest depth were selected to determine the maximum pit depth. Table 4.3. shows the maximum pitting depth for all samples.

Table 4.3. Maximum pit depth in microns (The maximum values were shown in Bold).

Maximum Pit Depth (μm)			
Test Samples	3 Days	15 Days	45 Days
Test Sample 1	13		
Test Sample 2	17		
Test Sample 3	15		
Test Sample 4		70	
Test Sample 5		80	
Test Sample 6		61	
Test Sample 7			100
Test Sample 8			89
Test Sample 9			76
Average	15	≈ 70	≈ 88

As a result of the three-day immersion test, the depth of the pitting corrosion caused by galvanic corrosion is around 15 microns and measured maximum pit depth for sample 2 is around 17 microns , as seen in Figure 4.14. The entire surface of the sectional sample was scanned, and it was observed that the place with the highest depth was formed near the junction.

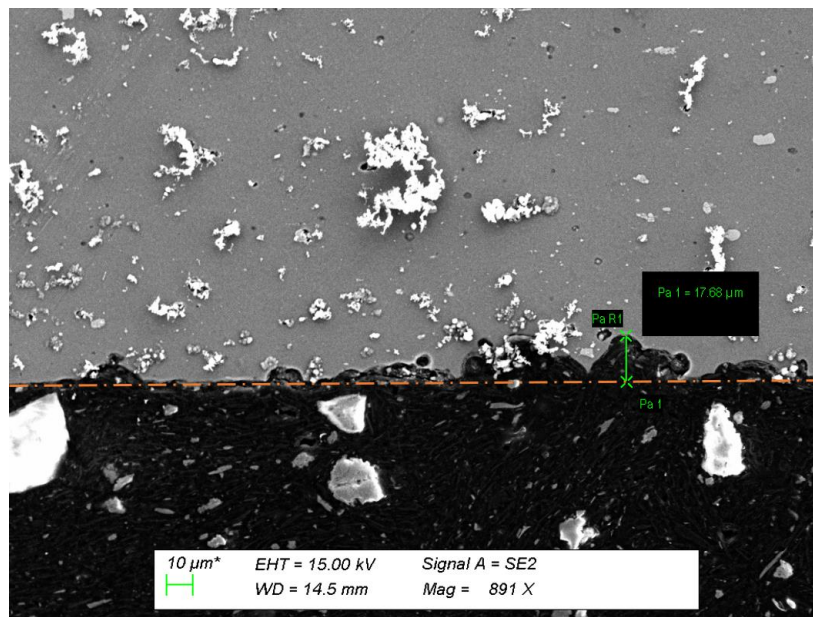


Figure 4.14. Maximum pit depth of sample 2 after 3 days immersion test.

When samples subjected to immersion test for fifteen days are examined, the average depth was around 70 microns and measured maximum pit depth for sample 5 seen in Figure 4.15 rises to around 80 microns in the sample with maximum pitting corrosion depth. Compared to the samples exposed to three days of immersion, it is seen that the density of corrosion is high. Corrosion products have filled the pits because, although polishing was done, the corrosion products remained in-depth as seen in the cross-sectional view of the sample.

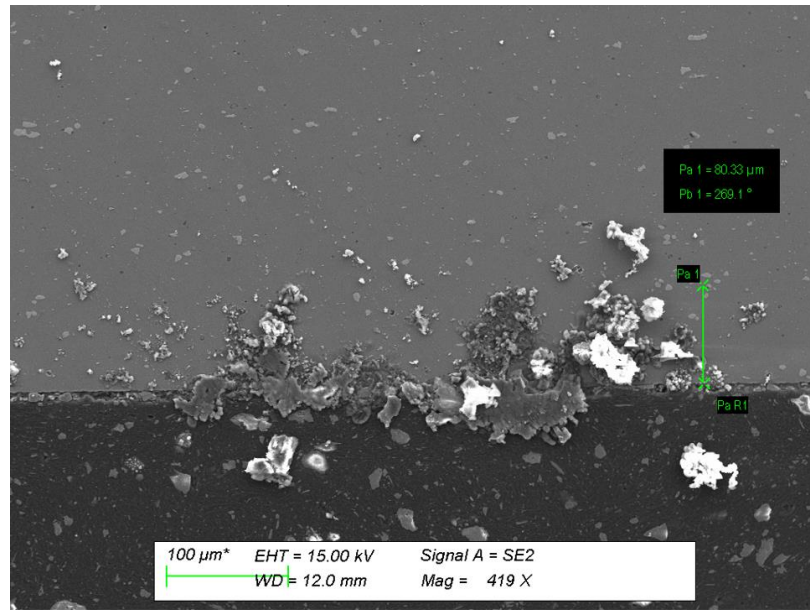


Figure 4.15. Maximum pit depth of sample 5 after 15 days immersion test.

As expected, the deepest pitting corrosion was observed in the samples subjected to the immersion test for the longest 45 days in the experimental planning. As can be seen in Figure 4.16, the maximum pit depth is around 100 microns. Although there is a two-fold increase compared to the depths of pitting corrosion formed as a result of the 15-day immersion test, it can be seen that the depth of corrosion does not increase linearly.

This situation can be explained as follows. Firstly, the Al(OH)_3 corrosion product, which is very difficult to dissolve, probably reduced the rate of the corrosion reactions. Secondly, as the pit corrosion progresses, the oxygen permeability becomes difficult or decreased [22]. Finally, the pit corrosion is reduced due to the passive layer formed by the aluminum material.

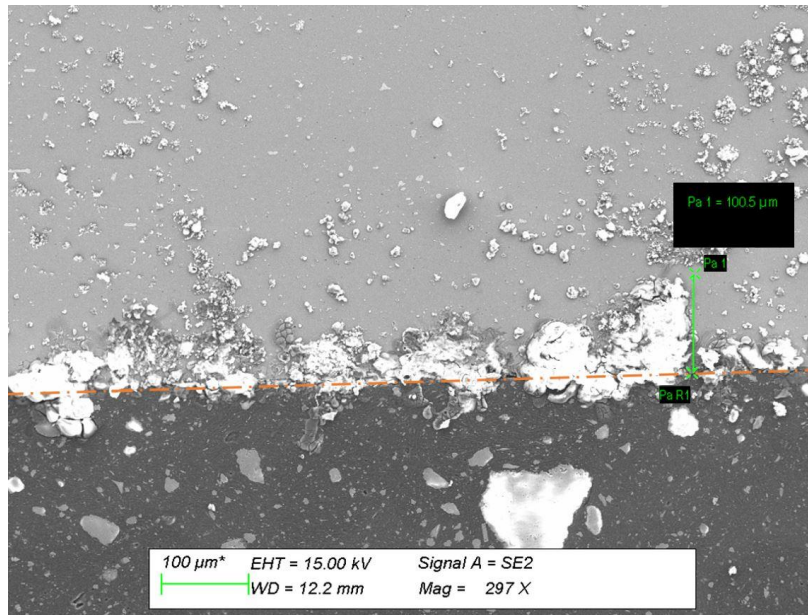


Figure 4.16. Maximum pit depth of sample 7 after 45 days immersion test.

Pit shape

According to the ASTM G-46 [55] (Examination and Evaluation of Pitting Corrosion), pitting corrosion patterns can be defined as elliptical (b), as shown in Figure 4.17, according to the 3-15 and 45 days of experiment results.

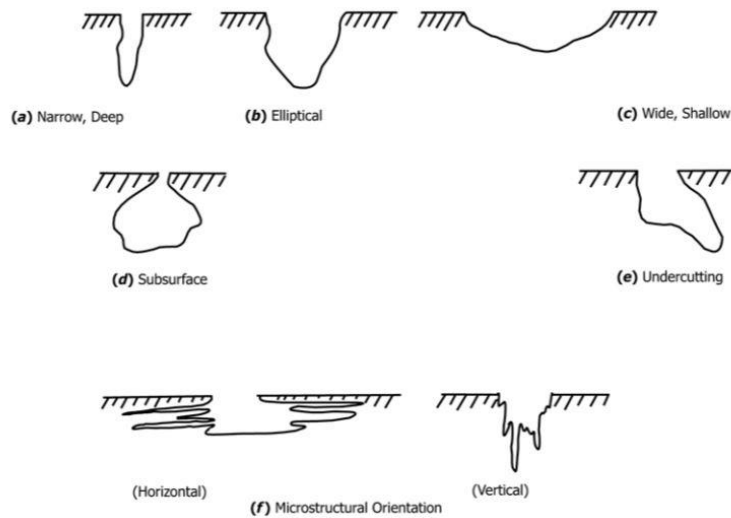


Figure 4.17. Pit shape standards according to ASTM G-46 [55].

Kinetic Modeling

According to Godard's model [56], the change in the pitting corrosion depth on aluminum material depending on time can be estimated according to the following equation.

$$d_{max.} = C(t)^{1/3} \quad (31)$$

Where;

d is the maximum pit depth

t is the time

C is the parameter related to the material and environment combination

It is possible to observe the change in the pitting corrosion depth that may constitute a structural hazard on the material. The graphic given in Figure 4.18 shows how the created equation changes over time.

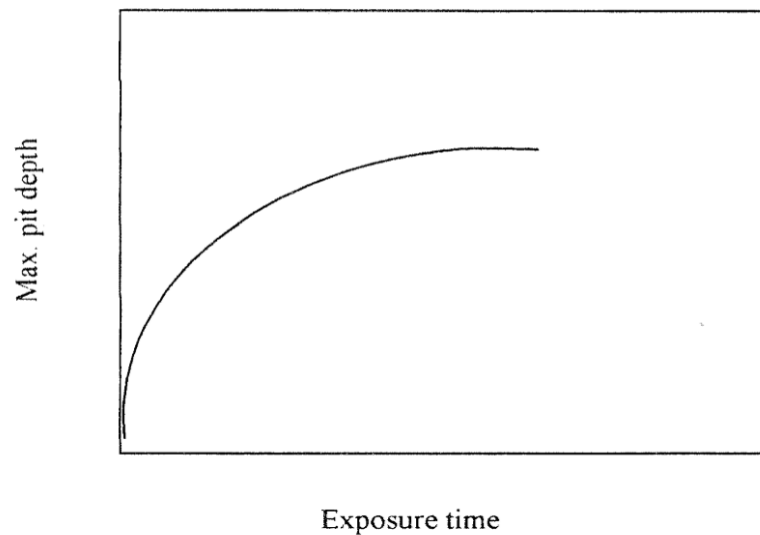


Figure 4.18. Godard's model relationship between maximum pit depth and exposure time [56].

According to Godard's model, if the maximum experimental depth of pitting corrosion as shown in Table 4.4. is placed into the equation over time, the following equations are obtained when d_{max} is in microns and t is in days.

Table 4.4. Maximum pit depths result for Godard's model.

Sample No	Time	Max. Pit Depth
Sample 2	3 Days	17 microns
Sample 5	15 Days	80 microns
Sample 7	45 Days	100 microns

In order to produce a kinetic model from the data obtained, the equations that were roughly deduced from Godard's model were combined in a single equation as follows.

$$d_{max} = 28t^{1/3} \quad (32)$$

C value is **28** for this test setup parameter related to the material and environment combination. Where d_{max} is in microns and t is in days. When d_{max} vs. t graph is drawn, a curve similar to Godard's model is obtained as shown in Figure 4.19. This curve shows that the pitting corrosion rate will decrease with increasing time.

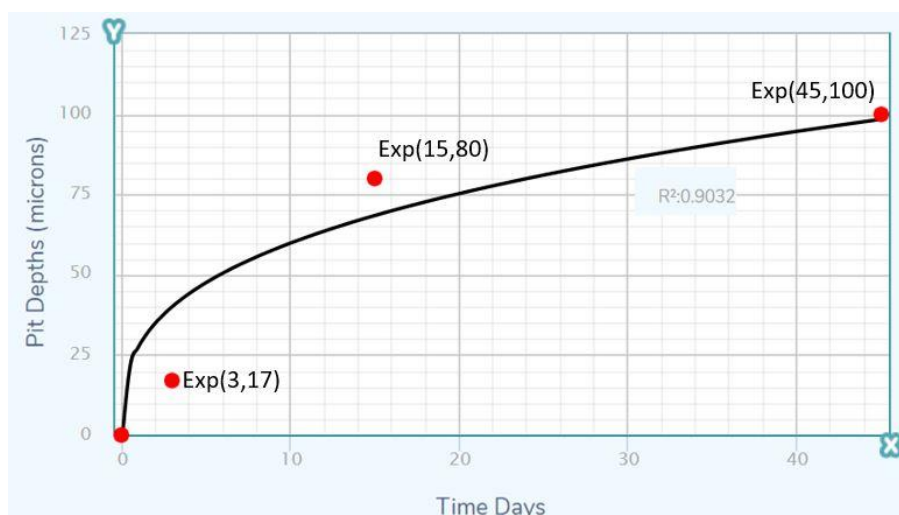


Figure 4.19. Fitting experimental data to the kinetic model.

Characterization of Pits

In order to confirm the pitting corrosion resulting from the immersion tests, the elemental mapping was performed using the EDS mapping method as an example from the SEM photograph shown in Figure 4.20 below. As can be seen from the test result, the corrosion products which show oxide formation as $\text{Al}(\text{OH})_3$, appearing on the aluminum material as green area.

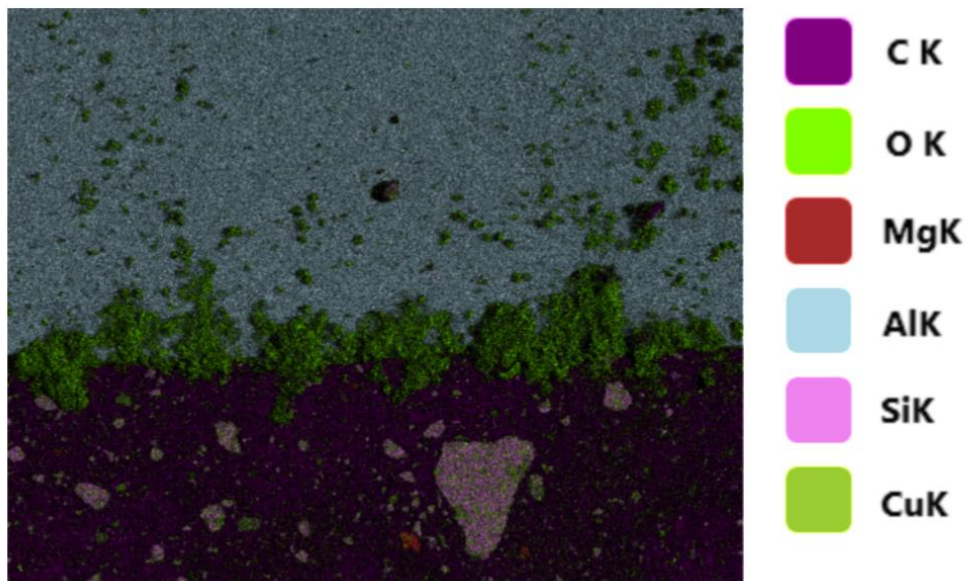


Figure 4.20. Elemental mapping analysis of pit depth area.

4.3. Simulation Results and Validation of Numerical Model

4.3.1. Local Current Density

Local current density distribution on AA2024-T3 and CFRP surface especially on joint for 3, 15 and 45 days were calculated by using Comsol Multiphysics software can be seen in Figure 4.21. As expected, the current density curves appear to be the highest 1.6 A/m^2 ($1.6\text{E-}4 \text{ A/cm}^2$) at the junction where the galvanic corrosion is most intense. This is very close to mixed potential theoretical value $1.5\text{E-}4 \text{ A/cm}^2$, confirms

the modeling results. The galvanic current density values that occur as it moves away from the junction decreases and approaches zero as the distance increases.

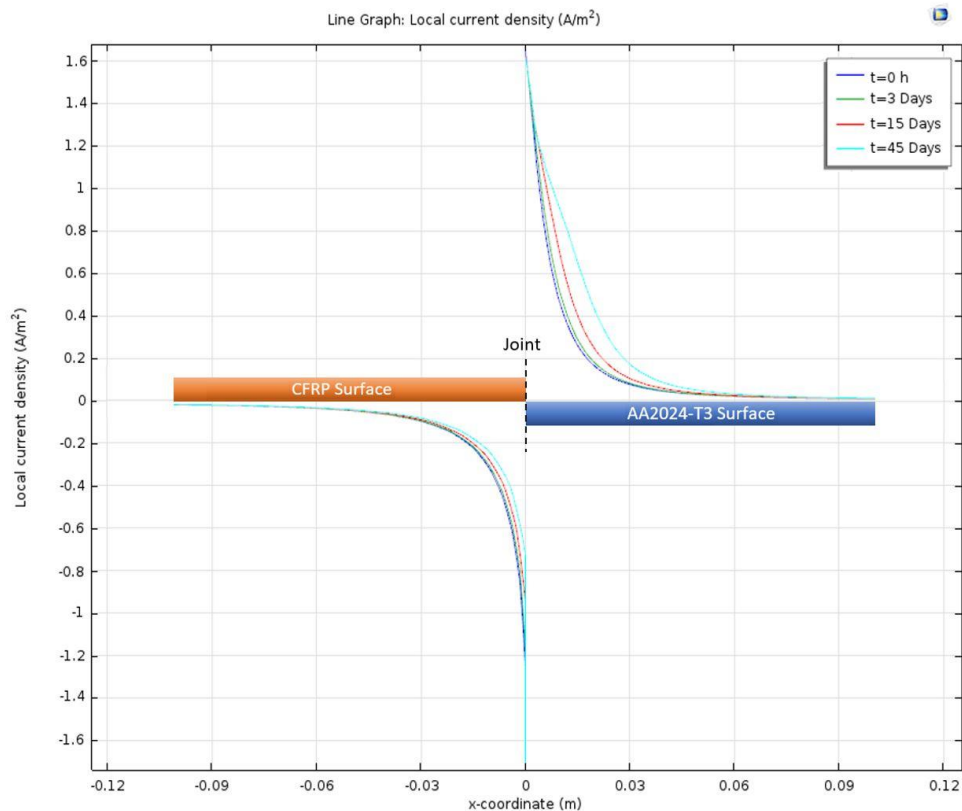


Figure 4.21. Local corrosion current density distribution on 2024-T3 and CFRP surfaces distribution calculated by using Comsol Multiphysics software.

As a result of potentiodynamic polarization experiments on aluminum alloy, the critical local corrosion current density required for the formation of stable pitting corrosion was found to be 1 A/m^2 ($1.0\text{E-}4 \text{ A/cm}^2$) as shown in Figure 4.3. From the modeling, corrosion current density value was observed to be reached on aluminum alloy near the junction point.

Part of Figure 4.21 was expanded to show calculated pit distances in Figure 4.22 as 4500 microns for a 3 days, 6000 microns for a 15 days, and about 7900 microns for a 45 days immersions. This does not mean that pit corrosion will not occur when the critical current density is below 1 A/m^2 ($1.0\text{E-}4 \text{ A/cm}^2$). But this formation will be at

the level called metastable. On the critical current density, we can see from the results of potentiodynamic polarization tests that when the critical current density value is exceeded, the self-formed passive protection layer of aluminum alloys will deteriorate and cause stable pitting corrosion.

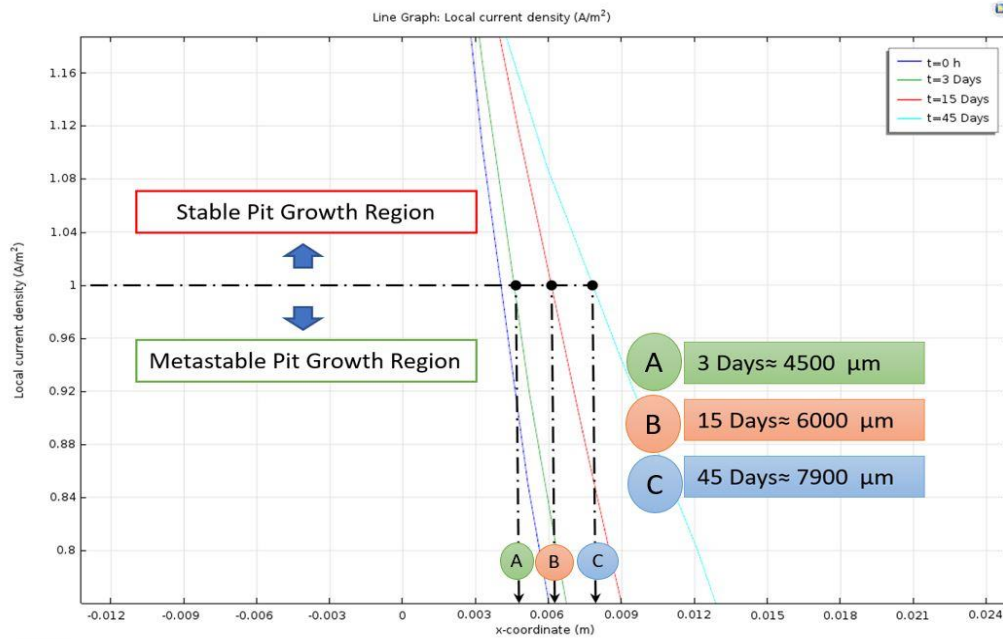


Figure 4.22. Local corrosion current density distribution on 2024-T3 and CFRP surfaces distribution in zoom view with stable and metastable region. Point A (4500 microns), Point B (6000 microns), and Point C (7900 microns) represent the critical pit distances from the joint for 3, 15, and 45 days respectively.

4.3.2. Surface Electrolyte Potential

Surface electrolyte potential distribution of the joint with different time are shown in Figure 4.23-26. From the results of the mixed potential theory application, -0.4 V (SCE) was expected as the galvanic corrosion potential, as shown in Figure 4.5. When looking at the junction on the model shown in the expanded view of the junction in - Figure 4.24-26. for 3, 15 and 45 days, the value of yellow color is seen between approximately -0.38 and -0.42 volts. Therefore, the mixed potential value calculated from the results of experimental polarization curves was confirmed by modeling the

electrolyte potential near the junction. It is necessary to examine the change in the electrolyte surface over time in order to understand maximum pitting corrosion depth through modeling.

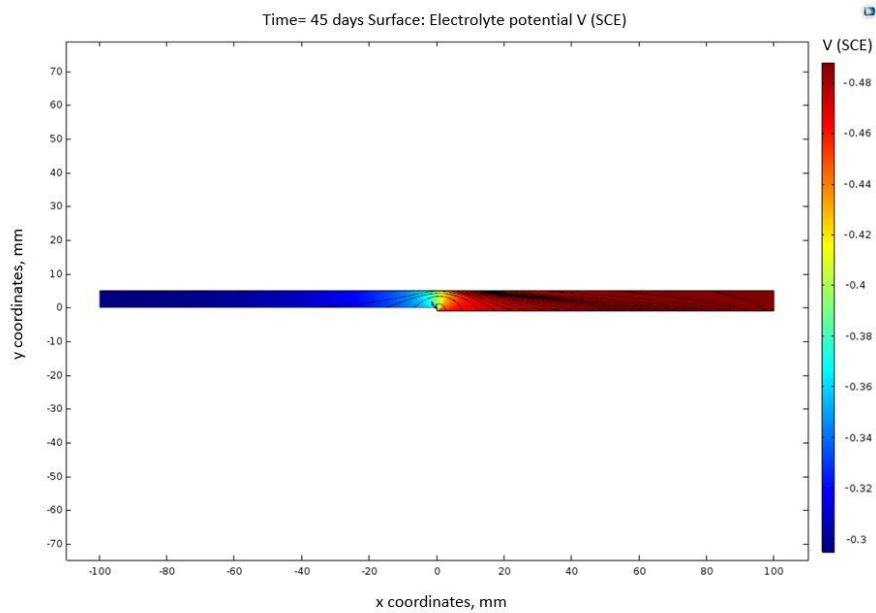


Figure 4.23. Surface electrolyte potential distribution at T=45 Days.

The change in the electrolyte potential over the surface with time is given in Figure 4.24-26.

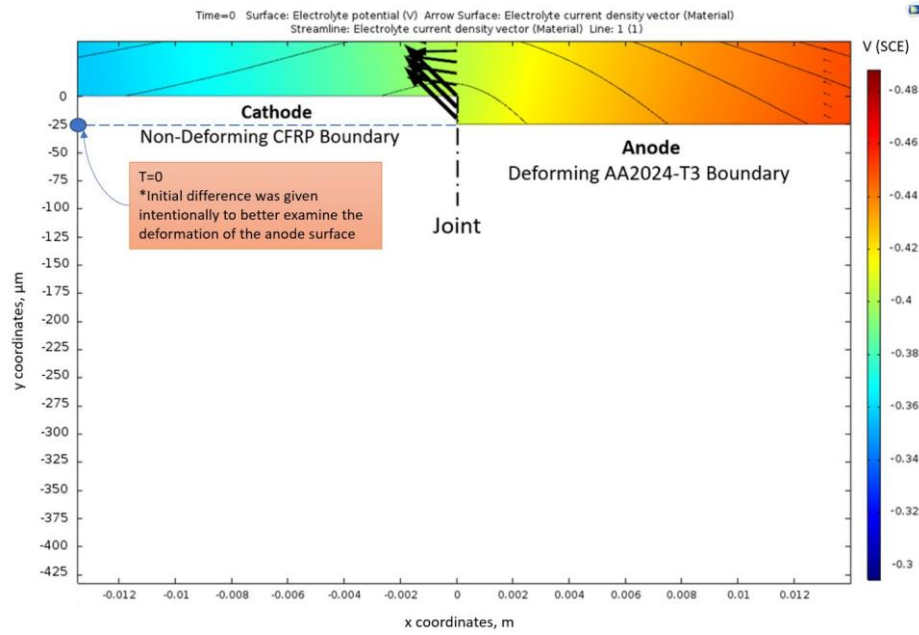


Figure 4.24. Deformation on AA2024-T3 boundary and surface electrolyte potential distribution at T=0 Days.

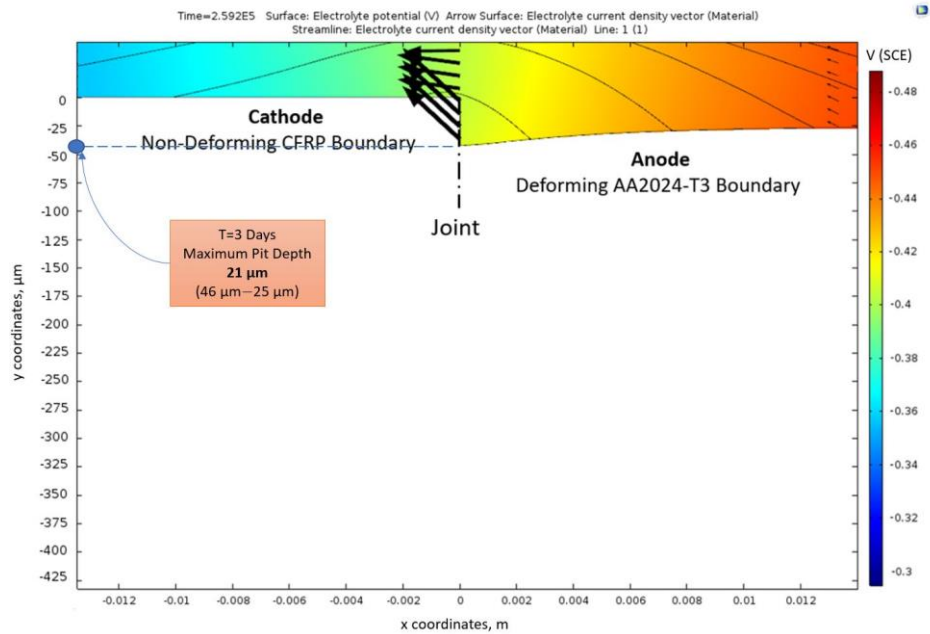


Figure 4.25. Deformation on AA2024-T3 boundary and surface electrolyte potential distribution at T=3 Days.

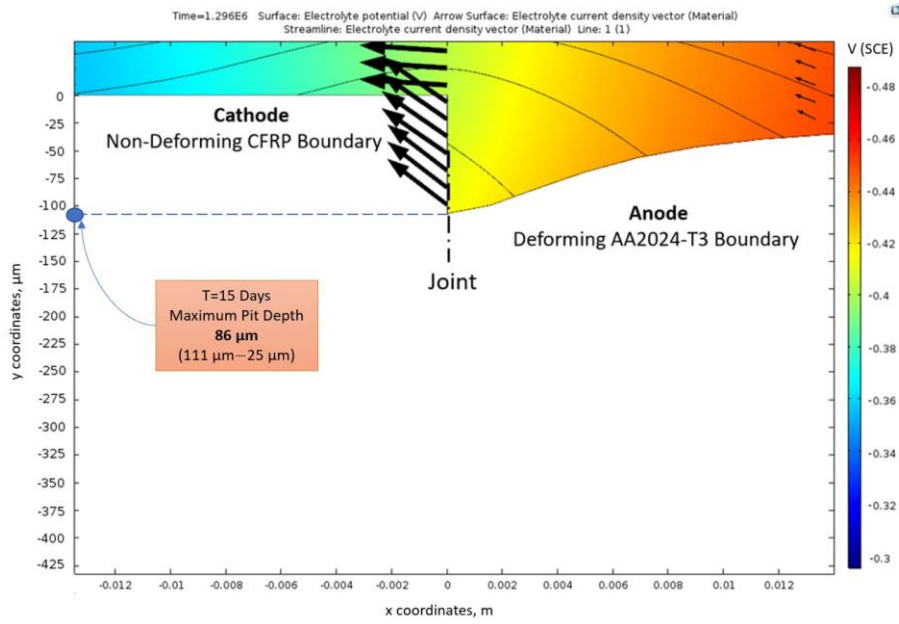


Figure 4.26. Deformation on AA2024-T3 boundary and surface electrolyte potential distribution at T=15 Days.

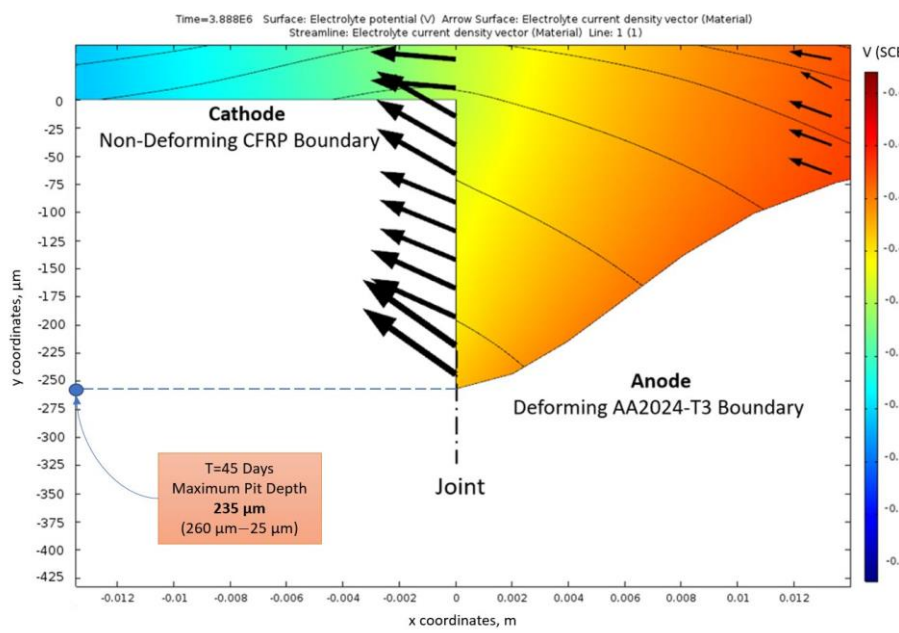


Figure 4.27. Deformation on AA2024-T3 boundary and surface electrolyte potential distribution at T=45 Days.

On the CRFP part, which is the cathodic side, the surface of the material has not been deformed, so no change has been made on the surface. Electrolyte solution caused corrosion on the surface of the material due to the reactions on the aluminum surface as expected.

The arrows at the junction point in Figure 4.24-26. indicate the direction of the current formed. The most largest depth of corrosion is observed at the end of 45 days, which was the longest duration in this study. It is observed that the galvanic corrosion effect decreased as we move away from the junction point at all time intervals.

When the critical pit distance and maximum pit depth calculated from the model and the result of immersion tests are compared, it can be seen that the modeling results are higher than the actual experimental data, as shown in Figure 4.28 and Figure 4.29, respectively.

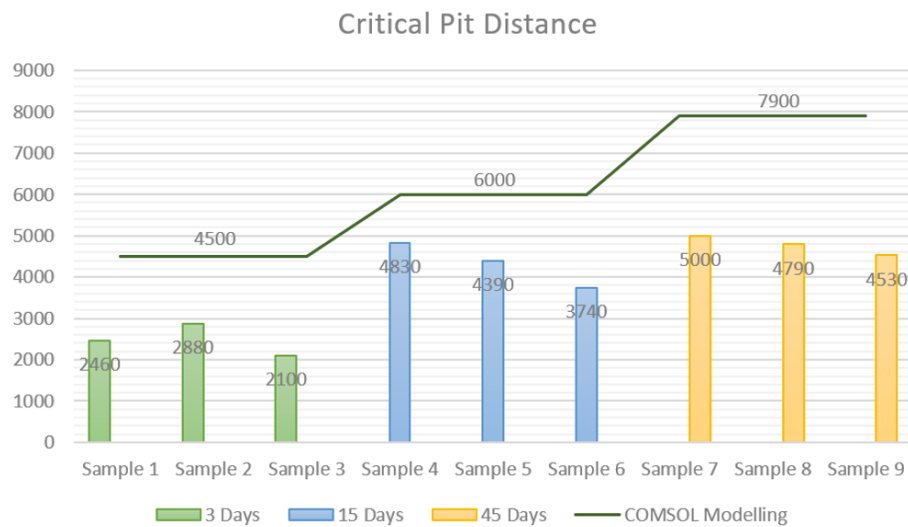


Figure 4.28. Comparison of critical pit distance results between modelling (shown with line) and immersion test (shown with bars).

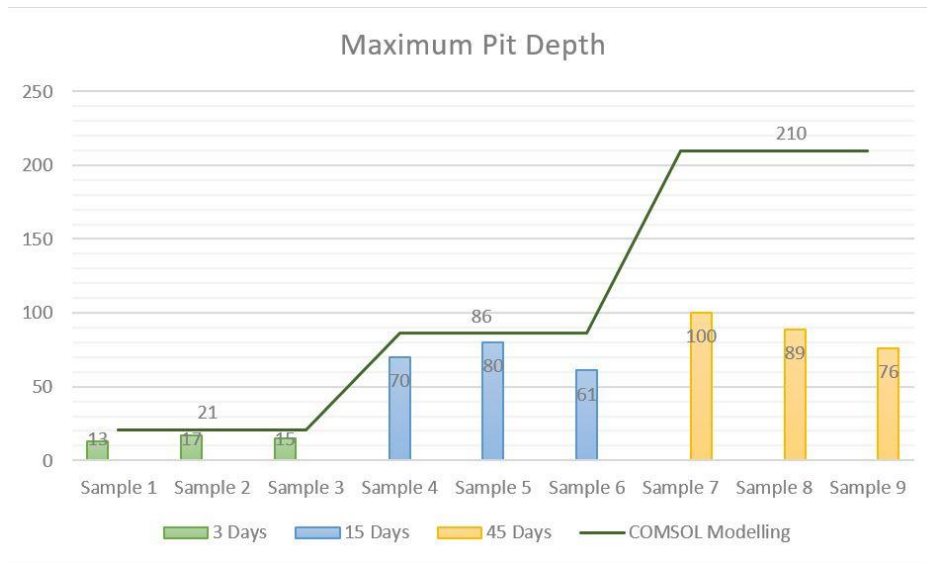


Figure 4.29. Comparison of maximum pit depth results between modelling (shown with line) and immersion test (shown with bars).

Figure 4.30 shows the difference between the model and experimental results given as percent of the value calculated from the model. When looking at the results, the closest values to the experimental results were obtained in 15 days, both in terms of critical pitting corrosion distance (%20) and maximum pitting depth (%7). It can be said that the passive layer formed by the aluminum continuously slows down the rate of corrosion formation in the 3 days experiment. Furthermore, It can be said that $\text{Al}(\text{OH})_3$ compound, which forms as time progresses and also dissolves difficultly, is one of the main factors that stop the continuous progress of corrosion. In addition, the corrosion formation will decrease after a certain depth as the pitting corrosion occurs, and the oxygen permeability decreases as the degree of corrosion increases. Since these effects could not be simulated in the model, the data obtained as a result of 15 days immersion gave the closest results to the modeling.

Numerical Model Over Predicts

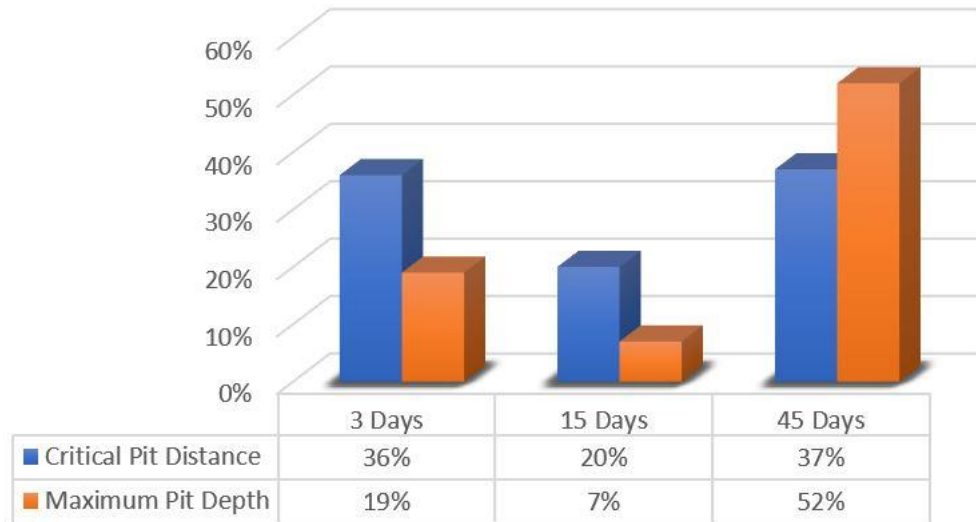


Figure 4.30. Convergence of modeling to experimental values.

Considering the correlations between critical pitting corrosion distance and maximum pitting corrosion depths, it is seen that the samples with high critical corrosion distance in the 3-day (sample 2) and 45-day (sample 7) tests also have the maximum pitting depths. However, the maximum pitting corrosion depth of the sample, which has the most critical pitting corrosion distance in 15-day samples, does not have the same value. Although this correlation was observed in 3-day and 45-day corrosion samples, the absence of that in 15-day samples prevents the conclusion that there is a clear correlation between these two factors. The critical pitting corrosion distance is mostly related to the intensity of the electric field formed between the galvanic couple [57]. However, the oxygen permeability and the passive layer formed by the aluminum alloy itself are more effective in the pitting corrosion progression. In addition, the corrosion products formed in the pit prevent the corrosion to go deeper there.

Discrepancies between the theoretically and experimentally obtained results for critical pit distance and maximum pit depth may be due to:

- 1) Different corrosion reactions that may be occurring in the secondary phases of aluminum alloy are neglected in the model.
- 2) It is assumed that there is no concentration change in the electrolyte solution during corrosion.
- 3) Dissolution reactions were assumed to be only on the anodic surface, and those on the cathodic surface were neglected.
- 4) The current density differences between the lower part and the upper part of the formed pit were neglected and the current value of the corrosion formed was taken as a constant.
- 5) Presence of Al^{+3} and OH^- ions formed during corrosion were neglected to affect the permeability of the electrolyte directly.
- 6) Especially in pitting formation, decrease in oxygen permeability and its effect on the rate of corrosion reaction was neglected.
- 7) The incubation time of chloride ions to the surface and the local dissolution time of the passive protective layer on aluminum material were unknown.

CHAPTER 5

CONCLUSION

The following conclusions can be drawn from the study of developing and verifying the finite element modeling method depending on the time (3-15-45 days) of galvanic corrosion occurring in the connection area between aluminum AA2024-T3 and CFRP material in %5 NaCl solution:

- With the potentiodynamic polarization measurements made separately for aluminum AA2024-T3 and CFRP, important parameters showing the corrosion behavior of the materials have been used effectively in galvanic corrosion modeling.
- The current and potential values of the galvanic couple found as a result of modeling. The potential result is between -0.38 V and -0.42 V and the current density curves appear to be the highest $1.6\text{E-}4 \text{ A/cm}^2$ at the junction where the galvanic corrosion is most intense. This is very close to mixed potential theory current density value $1.5\text{E-}4 \text{ A/cm}^2$ and potential value is -0.4 V supported the theory by giving a close result to the current and potential values found through the mixed potential theoretical.
- The closest results of the immersion tests performed for 3, 15 and 45 days in terms of both the critical pitting corrosion distance and the maximum pitting depth values are seen in the tests performed for 15 days. As can be seen from this result, there is an optimum time value for modeling corrosion kinetics.
- When all the test durations are evaluated on the test samples, it is seen that there is no clear correlation between the critical pitting corrosion distance and the maximum pitting depth.

In summary, the model developed for galvanic corrosion occurring in a harsh aircraft environment between aluminum AA2024-T3 and CFRP material, provides adequate

correlation with experimental results. The model can be used not only for this material pair but also for numerous galvanic couples.

REFERENCES

- [1] M. J. Benzakein, "What does the future bring? A look at technologies for commercial aircraft in the years 2035–2050," *Propuls. Power Res.*, 2014, pp. 166–170
- [2] T. Dursun and C. Soutis, "Recent developments in advanced aircraft aluminium alloys," *Mater. Des.*, vol. 56, pp. 862–871, 2014.
- [3] D. F. O. Braga, S. M. O. Tavares, L. F. M. Da Silva, P. M. G. P. Moreira, and P. M. S. T. De Castro, "Advanced design for lightweight structures: Review and prospects," *Prog. Aerosp. Sci.*, vol. 69, pp. 29–39, 2014.
- [4] H.M. Flower, *High Performance Materials in Aerospace*, Springer Science & Business Media, 2012.
- [5] M. Peters, C. Leyens, *Aerospace and space materials*, *Mater. Sci. Eng.* 3 (2009) 1–11.
- [6] L. Zhu, N. Li, and P. R. N. Childs, "Light-weighting in aerospace component and system design," *Propuls. Power Res.*, 2018.
- [7] M.L. Zheludkevich, S. Kallip, M. Serdechnova, *Protection of multimaterial assemblies*, *Phys. Sci. Rev.* (2016) 73–101.
- [8] K. Boodhun and B. Y. R. Surnam, "Corrosion of Aircrafts - A Case Study in Mauritius," pp. 77–82, 2015.
- [9] H. P. Hack, "Galvanic corrosion," *Shreir's Corros.*, pp. 828–856, 2010.
- [10] George W. Breen, "Aircraft Scheduled Structural Maintenance Programs: Current Philosophies And Methods In The United States And Their Applicability To The Royal Australian Air Force," 1995.
- [11] S. Srinivasan, "Computer Technology for Corrosion Assessment and Control," *Uhlig's Corros. Handb. Third Ed.*, pp. 1033–1044, 2011.
- [12] R.S. Munn, *Computer Modeling in Corrosion*, vol. 1154, ASTM International (1992)
- [13] A. Peratta and R. Adey, "Modeling galvanic corrosion in multi-material aircraft structures," *NACE - Int. Corros. Conf. Ser.*, vol. 44, no. 0, 2013.
- [14] "R.A. Adey, S.M. Niku, *Computer modelling of galvanic corrosion*, ASTM Special Technical Publication, (1988), pp. 96–117."

- [15] J.X. Jia, G. Song, A. Atrens, Experimental measurement and computer simulation of galvanic corrosion of magnesium coupled to steel, *Adv. Eng. Mater.* 9 (2007) 65–74.
- [16] “F. Thébault, B. Vuillemin, R. Oltra, C. Allely, K. Ogle, Modeling bimetallic corrosion under thin electrolyte films, *Corros. Sci.* 53 (2011) 201–207.”
- [17] “N. Murer, R. Oltra, B. Vuillemin, O. Néel, Numerical modelling of the galvanic coupling in aluminium alloys: a discussion on the application of local probe techniques, *Corros. Sci.* 52 (2010) 130–139.”
- [18] K. B. Deshpande, “Validated numerical modelling of galvanic corrosion for couples: Magnesium alloy (AE44) mild steel and AE44 aluminium alloy (AA6063) in brine solution,” *Corros. Sci.*, vol. 52, pp. 3514–3522, 2010.
- [19] Y. Zhang, Y.-L. Chen, W.-J. Fan, C.-G. Wang, G.-X. Bian, and C. Y. Zhang, “Study on the galvanic corrosion of aluminum alloy single bolted lap joints in simulated atmospheres.”
- [20] S. R. Cross, S. Gollapudi, and C. A. Schuh, “Validated numerical modeling of galvanic corrosion of zinc and aluminum coatings,” 2014.
- [21] E. Håkansson, J. Hoffman, P. Predecki, M. Kumosa, The role of corrosion product deposition in galvanic corrosion of aluminum/carbon systems, *Corros. Sci.* 114 (2017) 10–16.
- [22] M. Mandel and L. Krüger, “Determination of pitting sensitivity of the aluminium alloy EN AW-6060-T6 in a carbon-fibre reinforced plastic/aluminium rivet joint by finite element simulation of the galvanic corrosion process,” *Corros. Sci.*, vol. 73, pp. 172–180, 2013.
- [23] S. Palani, T. Hack, J. Deconinck, and H. Lohner, “Validation of predictive model for galvanic corrosion under thin electrolyte layers: An application to aluminium 2024-CFRP material combination,” *Corros. Sci.*, vol. 78, pp. 89–100, 2014.
- [24] V. Kucera and E. Mattsson, “Atmospheric Corrosion of Bimetallic Structures,” in *Atmospheric Corrosion*, W. H. Ailor (Ed.), Wiley, New York, 1982, pp. 561–574.
- [25] Oldfield, J. W., "Electrochemical Theory of Galvanic Corrosion," *Galvanic Corrosion*, ASTM STP 978, H. P. Hack, Ed., American Society for Testing and Materials, Philadelphia, 1988, pp. 5-22.
- [26] Brenet, J. P. and Traore, K., *Transfer Coefficients in Electrochemical Kinetics*, Academic Press, London, 1971, p.36.
- [27] Pickett, D.J., *Electrochemical Reactor Design*, Elsevier, Amsterdam, The Netherlands, 1977, p.53.

- [28] Mansfeld, F., Corrosion, Vol. 27, "Area Relationships in Galvanic Corrosion", 1971, p. 436.
- [29] C. Wagner, W. Traud, On the interpretation of corrosion processes through superposition of electro- chemical partial processes and on the potential of mixed electrodes, Z. Elektrochem. 44 (1938) 391–393.
- [30] Munn, R. S., Materials Performance, Vol. 21, "Computational Corrosion Analysis for Design of Microelectronic Components Under Conditions of Atmospheric Corrosion", August 1982, p. 29.
- [31] "Galvanic Corrosion." [Online]. Available: <https://www.beasy.com/22-galvanic-corrosion.html?start=4>. [Accessed: 10-Nov-2019].
- [32] M. G. Fontana and N. D. Greene, Corrosion Engineering, 2nd ed., McGraw-Hill, New York, 1978, p. 32.
- [33] J. W. Fu, "Galvanic Corrosion Prediction and Experiments Assisted by Numerical Analysis," in Galvanic Corrosion, ASTM STP 978, H. P. Hack (Ed.), American Society for Testing and Materials, Philadelphia, PA, 1988, pp. 79–85.
- [34] R. A. Adey and S. M. Niku, "Computer Modelling of Galvanic Corrosion," in Galvanic Corrosion, ASTM STP 978, H. P. Hack (Ed.), American Society for Testing and Materials, Philadelphia, PA, 1988, pp. 96–117.
- [35] R. G. Kasper and C. R. Crowe, "Comparison of Localized Ionic Currents as Measured From 1-D and 3-D Vibrating Probes with Finite-Element Predictions for an Iron-Copper Galvanic Couple," in Galvanic Corrosion, ASTM STP 978, H. P. Hack (Ed.), American Society for Testing and Materials, Philadelphia, PA, 1988, pp. 118–135.
- [36] A. von Hehl and P. Krug, "Aluminum and Aluminum Alloys," *Struct. Mater. Process. Transp.*, pp. 49–112, 2013.
- [37] R. B. Mears, "Aluminum and Aluminum Alloys," in Corrosion Handbook, H. H. Uhlig (Ed.), sponsored by The Electrochemical Society, Wiley, New York, 1976, pp. 39–56.
- [38] M. Pourbaix, Atlas of Electrochemical Equilibrium in Aqueous Solutions, 2nd English ed., NACE International (Houston, Texas) and Centre Belge d'Etude de la Corrosion "CEBELCOR," (Brussels, Belgium), 1974, pp. 168–175.
- [39] E. H. Hollingsworth and H. Y. Hunsicker, "Corrosion of Aluminum and Aluminum Alloys", in Metals Handbook, 9th ed., Vol. 13, Corrosion, ASM International, Metals Park, OH, 1987, pp. 583–609.
- [40] P. M. Aziz, Corrosion, 12, 35 (1956)
- [41] I. L. Rosenfeld, Localized Corrosion, National Association of Corrosion

- Engineers, NACE International, Houston, TX, 1974, pp. 386–389.
- [42] H. Kaesche, “Pitting Corrosion of Aluminum and Intergranular Corrosion of Aluminum Alloys,” in *Localized Corrosion*, B. F. Brown, J. Kruger, and R.W. Staehle (Ed.), NACE International, Houston, TX, 1974, p. 516.
 - [43] M. C. Reboul, T. J. Warner, H. Maye, and B. Baroux, “A Ten–Step Mechanism for the Pitting Corrosion of Aluminum,” *Materials Science Forum*, Transtech Publications, Vols. 217–222, Switzerland 1996, pp. 1553–1558.
 - [44] D. C. Silverman, “Practical Corrosion Prediction Using Electrochemical Techniques,” *Uhlig’s Corros. Handb. Third Ed.*, pp. 1129–1166, 2011.
 - [45] Aluminium Alloy - QQ-A-250/5 Sheet specification
 - [46] R. Domingo, “AC 43-4B - Corrosion Control for Aircraft.”, Federal Aviation Administration, Advisory Circular, pp. 2.1–2.17, 2018.
 - [47] J. T. Staley, “Corrosion of aluminum aerospace alloys,” *Mater. Sci. Forum*, vol. 877, pp. 485–491, 2017.
 - [48] D.L.Jordan, “Principles Of Accelerated Corrosion Testing,” *Uhlig’s Corros. Handb.*, 2011.
 - [49] M. Definition, “Galvanic Corrosion with Electrode Deformation,” pp. 1–14, 2013.
 - [50] A. T. Olanipekun, A. E. Faola, K. E. Oluwabunmi, and T. L. Oladosu, “Galvanic Corrosion of a Mild Steel Bolt In A Magnesium Alloy (AZ91D) Plate Simulation Using Comsol Multiphysics,” *Int. J. Sci. Eng. Res.*, vol. 5, no. 6, pp. 1329–1332, 2014.
 - [51] J. Oliver, “Passivity” *J. Chem. Inf. Model.*, vol. 53, no. 9, pp. 1689–1699, 2013.
 - [52] H. Böhni, “Localized Corrosion of Passive Metals,” *Uhlig’s Corros. Handb. Third Ed.*, pp. 157–169, 2011.
 - [53] D. G. Enos and L. L. Scribner, “The Potentiodynamic Polarization Scan.”, Solartron analytical, Technical report.
 - [54] C. Ponce-De-León, C. T. J. Low, G. Kear, and F. C. Walsh, “Strategies for the determination of the convective-diffusion limiting current from steady state linear sweep voltammetry,” *J. Appl. Electrochem.*, vol. 37, no. 11, pp. 1261–1270, 2007.
 - [55] E. Corro and C. Test-, “Standard Guide for Examination and Evaluation of Pitting Corrosion 1,” vol. 12, no. June 1973, pp. 1–8, 2020.
 - [56] D. W. Hoepfner, “Pitting Corrosion: Morphology and Characterization,” *Framework*, vol. 25, pp. 5.1-5.16, 1985.

- [57] S. Kumar Thamida, “Modeling and simulation of galvanic corrosion pit as a moving boundary problem”, Computational Materials Science 65, 2012.